J. Fluid Mech. (2014), *vol.* 743, *pp.* 75–123. © Cambridge University Press 2014
doi:10.1017/jfm.2013.679

Three-dimensional flow structures in laminar falling liquid films

Georg F. Dietze[1,†], W. Rohlfs[2], K. Nährich[2], R. Kneer[2] and B. Scheid[3]

[1]Laboratoire FAST, CNRS, UPMC Université Paris 06, et Université Paris-Sud, Bâtiment 502, Campus Universitaire d'Orsay, 91405 Orsay, France

[2]Institute of Heat and Mass Transfer, RWTH Aachen University, Aachen 52056, Germany

[3]Laboratoire TIPs, Université Libre de Bruxelles, Bruxelles 1050, Belgium

(Received 14 June 2013; revised 29 September 2013; accepted 19 December 2013; first published online 4 March 2014)

Full numerical simulations of the Navier–Stokes equations for four cases of vertically falling liquid films with three-dimensional surface waves have been performed. Flow conditions are based on several previous experimental studies where the streamwise and spanwise wavelengths were imposed, which we exploit by simulating periodic wave segments. The considered flows are laminar but approach conditions at which intermittent wave-induced turbulence has been observed elsewhere. Working liquids range from water to silicone oil and cover a large interval of the Kapitza number ($Ka = 18$–3923), which relates capillary to viscous forces. Simulations were performed on a supercomputer, using a finite-volume code and the volume of fluid and continuum surface force methods to account for the multiphase nature of the flow. Our results show that surface waves, consisting of large horseshoe-shaped wave humps concentrating most of the liquid and preceded by capillary ripples on a thin residual film, segregate the flow field into two regions: an inertia-dominated one in the large humps, where the local Reynolds number is up to five times larger than its mean value, and a visco-capillary region, where capillary and/or viscous forces dominate. In the inertial region, an intricate structure of different-scale vortices arises, which is more complicated than film thickness variations there suggest. Conversely, the flow in the visco-capillary region of large-Ka fluids is entirely governed by the local free-surface curvature through the action of capillary forces, which impose the pressure distribution in the liquid film. This results in flow separation zones underneath the capillary troughs and a spanwise cellular flow pattern in the region of capillary wave interference. In some cases, capillary waves bridge the large horseshoe humps in the spanwise direction, coupling the two aforementioned regions and leading the flow to oscillate between three- and two-dimensional wave patterns. This persists over long times, as we show by simulations with the low-dimensional model of Scheid *et al.* (*J. Fluid Mech.*, vol. 562, 2006, pp. 183–222) after satisfactory comparison with our direct simulations at short times. The governing mechanism is connected to the bridging capillary waves, which drain liquid from the horseshoe humps, decreasing their amplitude and wave speed and causing them to retract in the streamwise direction. Overall, it is observed that spanwise flow structures (not accounted for in two-dimensional investigations) are particularly complex due to the absence of gravity in this direction.

Key words: interfacial flows (free surface), thin films

† Email address for correspondence: dietze@fast.u-psud.fr

https://doi.org/10.1017/jfm.2013.679 Published online by Cambridge University Press

1. Introduction

Vertically falling liquid films are encountered in chemical engineering applications such as distillation columns or falling-film evaporators for inspissation. In the latter case, the film develops over a long distance, and surface waves, occurring due to the gravity-driven Kapitza instability (Kapitza 1948), organize into a pattern of large-amplitude three-dimensional solitary waves, travelling more or less independently from one another (Alekseenko, Nakoryakov & Pokusaev 1994). The transition to this 'developed state' from a noisy inlet condition is associated with a hierarchy of two- and three-dimensional instabilities. A smooth vertically falling liquid film is unstable to two- and three-dimensional perturbations at all flow rates (Brooke Benjamin 1957, 1961). According to Squire's theorem (Squire 1933), which applies to this flow, two-dimensional waves dominate the early stages of wave development, creating initially saturated large wave humps, which are subsequently subject to two kinds of secondary instabilities (Liu, Paul & Gollub 1993; Cheng & Chang 1995): a two-dimensional instability that leads to coarsening of the saturated two-dimensional waves into a pattern of solitary waves (Chang *et al.* 1996*b*), and a three-dimensional instability that leads to spanwise modulations of the saturated two-dimensional waves (Joo & Davis 1992; Chang, Demekhin & Kopelevich 1993). Consequently, residual inlet noise or designed inlet modulations can cause two-dimensional saturated waves to directly transit to three-dimensional structures, bypassing the two-dimensional secondary instabilities. Conversely, when the falling film is significantly confined by sidewalls, as may be the case in experimental realizations, the lateral boundary conditions already impose a three-dimensional primary flow. Depending on the sidewall separation distance, this can cause any (quasi-)two-dimensional wave dynamics to be practically bypassed (Vlachogiannis *et al.* 2010; Georgantaki *et al.* 2011; Pollak, Haas & Aksel 2011).

The first experimental evidence of three-dimensional instability presented by Tailby & Portalski (1962) consisted of photographs of the naturally developing free surface of a water film. These evince a highly irregular three-dimensional interface topology far downstream of the inlet characterized by horseshoe-shaped wave crests preceded by capillary ripples. Neighbouring horseshoe waves either travel separately from one another or occur as spanwise modulations of a connected wave front. The transition of saturated waves from two- to three-dimensional wave dynamics can take two paths, depending on the ratio of spanwise to streamwise noise level at the inlet (Chang *et al.* 1994). At a sufficiently large spanwise noise level, saturated two-dimensional wave fronts distort into a checkerboard pattern of spanwise modulations, which are out of phase for successive wave fronts. If spanwise residual noise is weak, secondary instabilities dominate further evolution of a two-dimensional saturated wave, leading to the earlier described large solitary waves. These are stable with respect to two-dimensional perturbations but unstable to spanwise disturbances (Chang *et al.* 1994), deforming the two-dimensional wave fronts in the shape of horseshoes. As opposed to the checkerboard instability, the resulting (horseshoe-shaped) spanwise modulations on successive wave fronts are in phase, and the underlying instability is designated as synchronous (Liu *et al.* 1992; Liu, Schneider & Gollub 1995). If these modulations expand sufficiently downstream, they pinch off and travel as isolated three-dimensional disturbances (Petviashvili & Tsvelodub 1978; Alekseenko *et al.* 2005; Demekhin *et al.* 2007*b*) that may also interact in a more complex setting (Demekhin *et al.* 2010).

Evidence of these two evolution scenarios has been collected in a number of works. Trifonov (1990) differentiated the two three-dimensional instabilities

https://doi.org/10.1017/jfm.2013.679 Published online by Cambridge University Press

based on numerical solutions of Shkadov's integral boundary layer (IBL) model (Shkadov 1967). The same model was used by Demekhin *et al.* (2007*a*) in their thorough investigation of the linear and nonlinear transition from two- to three-dimensional wavy liquid films and later validated against experiments (Demekhin *et al.* 2010). Liu *et al.* (1992, 1995) proved the two scenarios experimentally and showed that high-frequency single-peaked waves develop checkerboard and waves with large separations develop synchronous spanwise patterns. A numerical confirmation of the synchronous evolution scenario was provided by the spatio-temporal direct numerical simulations (DNS) of Kunugi & Kino (2005). A clear picture of the wave topology resulting from synchronous instability was provided by the experiments of Park & Nosoko (2003). Here, a spatial excitation in the spanwise direction was imposed in addition to a temporal inlet disturbance of given frequency, allowing one to bypass the two-dimensional secondary wave dynamics and to produce three-dimensional waves of prescribed span- and streamwise wavelength near the inlet. We follow this approach in our work by way of numerical simulations of periodic wave segments. We have performed, on the one hand, full-scale DNS of the Navier–Stokes equations (limited to several wave periods) on the Juropa supercomputer at Forschungszentrum Jülich and, on the other hand, long-time simulations (up to 50 wave periods) using the low-dimensional weighted residual integral boundary layer (WRIBL) model of Scheid, Ruyer-Quil & Manneville (2006). We employ these simulations to address a number of open questions regarding the dynamics of three-dimensional falling liquid films.

Firstly, it is not clear how turbulence develops in such films. Ishigai *et al.* (1972) performed Reynolds' dye experiment for falling liquid films and identified three thresholds for the Reynolds number $Re = q_0/\nu_l$, where q_0 designates the total flow rate per unit width at the test section inlet and ν_l is the kinematic viscosity of the liquid. The first, $Re = 2.2Ka^{3/10}$, delimits the onset of 'wave-induced' turbulence, where the Kapitza number $Ka = \sigma/(\rho_l \nu_l^{4/3} g^{1/3})$ relates capillary and viscous forces in the liquid film, with σ the surface tension, ρ_l the liquid density and g the gravitational acceleration. The second is given by $Re = 75$ and marks the start of wall-induced turbulence. The third threshold $Re = 400$ (see also Brauer 1956) marks the onset of fully turbulent flow dominated by turbulence production at the wall. Below this value, Ishigai *et al.* (1972) observed the flow to be intermittently turbulent, which is related to the passage of surface waves, as was established experimentally by Adomeit & Renz (2000). The above introduced critical Reynolds number values are surprisingly low compared to single-phase channel flow, which is laminar for $Re < 675$, using half the channel height as length scale. The liquid film base flow being basically 'half a plane channel flow', the Reynolds numbers for the two flows can be directly compared. This shows that, although the thresholds of fully turbulent flow are not drastically different for film and channel flow (compare 400 and 675), the onset of turbulence occurs at much lower Reynolds number values for falling liquid films, i.e. at $Re = 75$. Our full numerical simulations come close to this threshold (the maximal Reynolds number studied is $Re = 59$) and have enabled us to identify a possible role of surface waves in the transition to intermittent turbulence.

Secondly, although it is known that three-dimensional surface waves intensify heat and mass transfer between film and wall as well as across the free surface (Alekseenko *et al.* 1994; Kunugi & Kino 2005; Demekhin *et al.* 2007*a*), underlying intensification mechanisms have not been fully elucidated. Our DNS evince a number of three-dimensional flow structures causing the intensification of convective transport within the film.

https://doi.org/10.1017/jfm.2013.679 Published online by Cambridge University Press

Finally, the mechanisms governing large and capillary wave structures have not been fully identified. Regarding the large wave humps, Demekhin *et al.* (2007*a*) proposed a Plateau–Rayleigh type of mechanism, resulting from the large streamwise interfacial curvature slightly downstream of the wave crest. Regarding the capillary waves, Park & Nosoko (2003) conjectured that the Plateau–Rayleigh instability may cause these to develop spanwise modulations. We investigate this by analysing the total free-surface curvature of the three-dimensional nonlinear wave structure as well as the associated pressure and flow fields.

Four cases of three-dimensional vertically falling liquid films are considered. Cases 1 and 2 correspond to experiments by Park & Nosoko (2003) (panels c and d in their figure 7), who employed water as working liquid and imposed spanwise and streamwise wavelengths with needles periodically submerged into the film. For these cases, the Kapitza number is very large ($Ka = 3923$) and the free surface is covered by a large number of capillary ripples. Case 3 corresponds to the flow conditions extrapolated from the two-dimensional experiments of Dietze, Al-Sibai & Kneer (2009), who used a dimethylsulphoxide (DMSO)–water solution as working liquid ($Ka = 509$). Case 4 corresponds to measurements performed in the same test set-up as Rohlfs *et al.* (2012) with silicone oil ($Ka = 18$). Here, viscous dissipation is the more relevant mechanism counteracting gravity and the film develops a very thin residual layer without capillary waves.

This article is structured as follows. Section 2 defines governing equations (§ 2.1) as well as boundary and initial conditions (§ 2.2) for the considered flow in a continuum setting. Section 3 specifies the set-up of our numerical simulations in terms of employed numerical methods and spatio-temporal discretization. Section 4 defines flow conditions for cases 1–4 in more detail (see tables 4 and 3) and compares our simulations with experiments. Analysis of numerical results is presented in § 5, which is subdivided into a first part (§ 5.1) dealing with wave dynamics, a second (§ 5.2) dealing with the velocity field within the film, and a third (§ 5.3) dedicated to the coupling of the two. (A fourth subsection (§ 5.4) provides a short description of the wave-induced gas flow.) In § 5.1, we make use of complementary simulations with the low-dimensional WRIBL model of Scheid *et al.* (2006) to investigate the long-time fate of three-dimensional wave structures. These simulations evince oscillating wave dynamics, for which a governing mechanism is identified in § 5.3 based on DNS data. Conclusions are drawn in § 6, while in the Appendix, WRIBL simulation results are scrutinized against our DNS.

2. Continuum description of the flow

As shown in figure 1, we study the flow of a vertical liquid film falling due to gravity in a quiescent gaseous atmosphere. We focus on periodic segments of the three-dimensional wavy flow, wavelengths in the streamwise (in line with gravity) and spanwise directions being denoted by Λ_x and Λ_z, while H designates the domain height, chosen to provide sufficient clearance above the surface waves. Owing to spanwise symmetry (shown by the dotted line), only half of the box depicted in figure 1(*a*) is considered.

2.1. *Governing equations*

The flow in the liquid ($k = l$) and gas ($k = g$) is governed by the Navier–Stokes and continuity equations written here with Einstein's notation ($i, j = 1, 2, 3$ corresponding to coordinates x, y and z and velocity components u, v and w) in dimensionless form

https://doi.org/10.1017/jfm.2013.679 Published online by Cambridge University Press

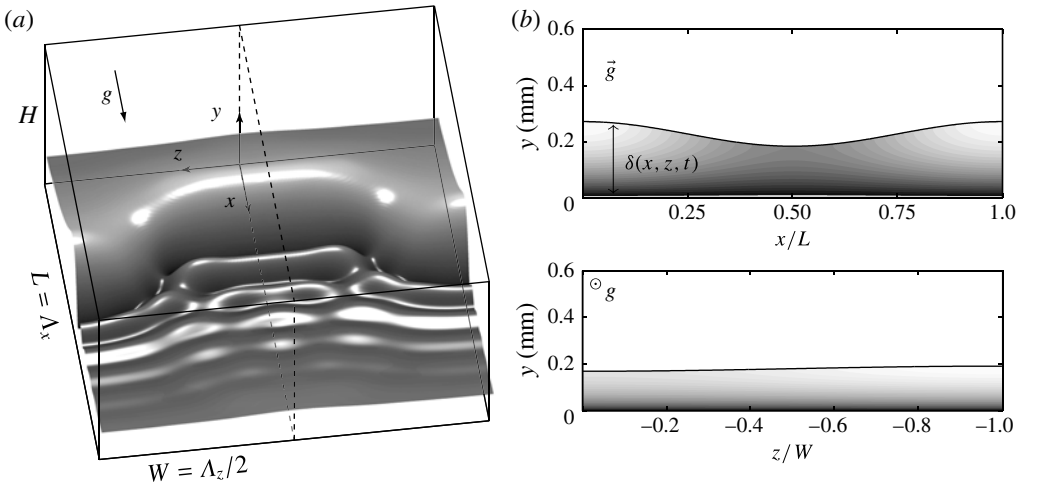


FIGURE 1. Three-dimensional periodic wave segment of a vertically falling liquid film as studied in this work. (*a*) Developed free-surface wave topology (owing to symmetry, the computational domain is limited to half the depicted box). (*b*) Initial ($t = 0$) film thickness distribution (for our DNS) seen in x–y ($z = 0$) and z–y ($x = \Lambda_x/2$) slices. Grey shades indicate the streamwise velocity component.

denoted with a tilde, introducing the Reynolds and Froude numbers Re and Fr:

$$\left.\begin{gathered}\partial_{\tilde{t}}\tilde{u}_i + \tilde{u}_j\partial_{\tilde{x}_j}\tilde{u}_i = -\partial_{\tilde{x}_i}\tilde{p} + \frac{X_k}{Re}\,\partial_{\tilde{x}_j\tilde{x}_j}\tilde{u}_i + \frac{\delta_{i1}}{Fr^2}, \quad \partial_{\tilde{x}_j}\tilde{u}_j = 0, \\ X_l = 1, \quad X_g = \frac{\Pi_\rho}{\Pi_\mu}, \quad Re = \frac{\rho_l U_0 \delta_0}{\mu_l} = \frac{q_0}{\nu_l}, \quad Fr = \frac{U_0}{g^{1/2}\delta_0^{1/2}} = \left[\frac{Re}{3}\right]^{1/2},\end{gathered}\right\} \tag{2.1}$$

where U_0 and δ_0 (δ_{ij} designates the Kronecker symbol) denote the mean velocity and thickness of a smooth falling film (Nusselt 1923) of flow rate q_0, corresponding to the open-domain experiment that we wish to reproduce. They represent the velocity and length scales for non-dimensionalization. The time scale is given by δ_0/U_0 and pressure is non-dimensionalized with $U_0^2\rho_k$, while $\Pi_\rho = \rho_g/\rho_l$ and $\Pi_\mu = \mu_g/\mu_l$. At the free surface, $y = \delta(x, z, t)$, continuity of velocity and normal and tangential stress balances yield four interfacial coupling conditions in addition to the so-called kinematic condition (relating free-surface velocity and film thickness δ):

$$\left.\begin{gathered}\tilde{u}_l = \tilde{u}_g, \quad \tilde{v}_l = \tilde{v}_g = \partial_{\tilde{t}}\tilde{\delta} + \tilde{u}_l\partial_{\tilde{x}}\tilde{\delta} + \tilde{w}_l\partial_{\tilde{z}}\tilde{\delta}, \\ \left[\tilde{S}_{ij}^l \cdot n_j\right] \cdot n_i = \Pi_\rho[\tilde{S}_{ij}^g \cdot n_j] \cdot n_i + We\tilde{\kappa}, \quad [\tilde{S}_{ij}^l \cdot n_j] \cdot \tau_i^m = \Pi_\rho[\tilde{S}_{ij}^g \cdot n_j] \cdot \tau_i^m,\end{gathered}\right\} \tag{2.2}$$

where the orthonormal surface coordinate system ($\boldsymbol{n}$, $\boldsymbol{\tau}^m$, $m = 1, 2$) was introduced:

$$\left.\begin{gathered}\boldsymbol{n} = [-\partial_x\delta,\, 1,\, -\partial_z\delta](1 + (\partial_x\delta)^2 + (\partial_z\delta)^2)^{-1/2}, \\ \boldsymbol{\tau}^1 = [1,\, \partial_x\delta,\, 0](1 + (\partial_x\delta)^2)^{-1/2}, \quad \boldsymbol{\tau}^2 = [0,\, \partial_z\delta,\, 1](1 + (\partial_z\delta)^2)^{-1/2}.\end{gathered}\right\} \tag{2.3}$$

The Weber number We (relating capillary forces and inertia) and the dimensionless curvature of the free surface $\tilde{\kappa}$ are defined as

$$We = \frac{\sigma}{\rho_l\delta_0 U_0^2}, \quad \tilde{\kappa} = \kappa\delta_0, \quad \kappa = -\boldsymbol{\nabla}\cdot\boldsymbol{n}. \tag{2.4}$$

https://doi.org/10.1017/jfm.2013.679 Published online by Cambridge University Press

Finally, $\tilde{S}_{ij}^k$ designates the dimensionless stress tensors of liquid and gas:

$$\tilde{S}_{ij}^k = S_{ij}^k \frac{1}{\rho_k U_0^2}, \quad S_{ij}^k = \mu_k(\partial_{x_j} u_i + \partial_{x_i} u_j) - \delta_{ij} p_k. \tag{2.5}$$

2.2. *Boundary and initial conditions*

Expressions in this section are written in dimensional form in order to clearly identify the parameters controlling our numerical simulations. We impose spanwise symmetry and streamwise periodicity at the corresponding limits of the domain shown in figure 1(*a*), while no-slip and no-penetration conditions are prescribed at the bottom wall:

$$\partial\varphi/\partial z|_{z=0} = \partial\varphi/\partial z|_{z=\Lambda_z/2} = 0, \quad \varphi|_{x=0} = \varphi|_{x=\Lambda_x}, \quad u_i|_{y=0} = 0, \tag{2.6}$$

where φ may designate any one of the variables u, v, w and p. As initial conditions for the film thickness distribution and liquid streamwise velocity profile, we set

$$\delta|_{t=0} = \bar{\bar{\delta}}[1 + \varepsilon_x \cos(k_x x) + \varepsilon_z \cos(k_z z)], \quad u_l = \frac{\delta^2 g}{\nu_l}\left(\frac{y}{\delta} - \frac{1}{2}\frac{y^2}{\delta^2}\right), \tag{2.7}$$

where $k_x = 2\pi/\Lambda_x$, $k_z = 4\pi/\Lambda_z$ and $\varepsilon_x = 0.2$, $\varepsilon_z = 0.05$, imposing a mainly two-dimensional wave modulated by a small-amplitude spanwise disturbance (see figure 1*b*) as well as a gravity-driven locally parabolic velocity profile in the film (the other velocity components are initially set to $v = w = 0$ but, along with u, adjust to the imposed three-dimensional topology within the first numerical iteration to satisfy the conservation equations).

While initial conditions are more or less irrelevant for simulations using an open domain (owing to the convective nature of the film instability), they play an important role when streamwise periodic boundary conditions are employed (closed domain), as done here. In this case, the initial film thickness distribution in (2.7) fixes the liquid volume V_l in the computational box, which subsequently remains unchanged throughout the simulation, owing to the conservative nature of the employed finite-volume discretization method. For given domain dimensions and fluid properties, V_l controls the Reynolds number and wave frequency of the film flow (the two are coupled in this case). The quantity $\bar{\bar{\delta}}$ in (2.7) thus becomes an important control parameter of the simulation, as it fixes the liquid volume $V_l = \bar{\bar{\delta}}\Lambda_x\Lambda_z$. It represents the mean film thickness $\bar{\bar{\delta}} = \Lambda_x^{-1}\Lambda_z^{-1}\int_0^{\Lambda_z}\int_0^{\Lambda_x}\delta\,\mathrm{d}x\,\mathrm{d}z$, which would normally be considered an output parameter. Indeed, $\bar{\bar{\delta}}$ is *a priori* unknown for a required set of flow conditions (expressed in terms of the set $\{Re, \Lambda_x, \Lambda_z\}$, $\{f, \Lambda_x, \Lambda_z\}$ or $\{Re, f, \Lambda_z\}$). Accordingly, for our simulations, $\bar{\bar{\delta}}$ was estimated based on an iteration of preliminary two-dimensional simulations with the goal of matching the targeted values for Reynolds number Re^{tgt} and wave frequency f^{tgt} as closely as possible (here, the superscript '*tgt*' was introduced to designate a target value). Target values for different flow parameters are reported in table 3 in § 4 for the four cases considered in this work and will be discussed later in more detail. Meanwhile, table 1 compares Re^{tgt} and f^{tgt} with values actually achieved in our three-dimensional DNS (the wave frequency from DNS was computed by evaluating the instantaneous wave celerity through cross-correlation of wave profiles and invoking $f = c/\Lambda_x$). In a closed-domain simulation, the Reynolds number is not controlled explicitly and evolves over time,

https://doi.org/10.1017/jfm.2013.679 Published online by Cambridge University Press

Case	Re^{tgt}	f^{tgt} (Hz)	δ_0^{tgt} (μm)	$\bar{\bar{\delta}}$ (μm)	$\delta_0^{tgt}/\bar{\bar{\delta}}$	Re_{DNS}^{max}	f_{DNS}^{max} (Hz)
1	40.8	19.1	215.1	196.75	1.10	41.3	19.7
2	59.3	17.0	243.6	220.05	1.11	57.6	18.9
3	15.0	16.0	334.0	298.0	1.12	14.7	16.1
4	6.2	16.6	921.0	830	1.11	6.3	16.3

TABLE 1. Targeted and actually achieved values for different parameters of our periodic DNS. Here $Re^{tgt} = q_0/\nu_l$, f^{tgt} and $\delta_0^{tgt} = (3Re^{tgt}\nu_l^2/g)^{1/3}$ designate target values recorded in experiments used for validation in § 4 (see table 3), while Re_{DNS}^{max} and f_{DNS}^{max} designate actually achieved values corresponding to the time point of maximal Reynolds number (see figure 11 for a full history of Re_{DNS}). The quantity $\bar{\bar{\delta}} = \Lambda_x^{-1}\Lambda_z^{-1}\int_0^{\Lambda_z}\int_0^{\Lambda_x}\delta\,\mathrm{d}x\,\mathrm{d}z$ fixes the initial thickness distribution (2.7) and thus is a numerical control parameter.

starting from the initial condition. Its instantaneous value Re_{DNS} is obtained by spatially averaging the local instantaneous streamwise flow rate per unit width q_{lx} over the box size:

$$Re_{DNS} = \frac{\bar{\bar{q}}_{lx}}{\nu_l}, \quad \bar{\bar{q}}_{lx} = \frac{1}{\Lambda_x}\int_0^{\Lambda_x}\bar{q}_{lx}\,\mathrm{d}x, \quad \bar{q}_{lx} = \frac{2}{\Lambda_z}\int_0^{\Lambda_z/2} q_{lx}\,\mathrm{d}z, \quad q_{lx} = \int_0^{\delta} u\,\mathrm{d}y. \tag{2.8}$$

In table 1, we report Re_{DNS}^{max} and f_{DNS}^{max}, corresponding to the time point with largest Reynolds number value (see figure 11 for a full history of Re_{DNS}), which are in satisfactory agreement with Re_{DNS}^{tgt} and f_{DNS}^{tgt}.

3. Direct numerical simulations: methods and discretization

DNS of the four cases were performed using the finite-volume code OpenFOAM (Rusche 2002), which is based on the volume of fluid (VOF) method first introduced by Hirt & Nichols (1981) to track the distribution of multiple phases, and the continuum surface force (CSF) method developed by Brackbill, Kothe & Zemach (1992) to account for the contribution of capillary forces at the liquid–gas interface. The code solves the Navier–Stokes equations for a single fluid on the periodic domain depicted in figure 1(*a*) (the computational domain corresponds to half the pictured box owing to spanwise symmetry), as well as the convective equation for the liquid volume fraction α, while enforcing a divergence-free velocity field (under the considered flow conditions, the gas is in good approximation incompressible):

$$\bar{\rho}\partial_t u_i + \bar{\rho}u_j\partial_{x_j}u_i = -\partial_{x_i}p + \bar{\rho}g_i + \bar{\mu}\partial_{x_jx_j}u_i + F'''_{\sigma i}, \tag{3.1a}$$

$$\partial_t\alpha + u_i\partial_{x_i}\alpha = 0, \quad \partial_{x_j}u_j = 0. \tag{3.1b}$$

The fluid properties of the single fluid are computed from the pure-phase properties weighted by the liquid volume fraction α:

$$\bar{\rho} = \alpha\rho_l + (1-\alpha)\rho_g, \quad \bar{\mu} = \alpha\mu_l + (1-\alpha)\mu_g. \tag{3.2}$$

Solving (3.1*b*) numerically requires special care in order to avoid the creation of flotsam due to numerical diffusion (Prosperetti & Tryggvason 2007). While other solvers achieve this by incorporating a piecewise linear geometrical discretization approach for the interface (Youngs 1982; Popinet 2009), the OpenFOAM code

https://doi.org/10.1017/jfm.2013.679 Published online by Cambridge University Press

Case	H (mm)	H_f (mm)	L (mm)	W (mm)	Δx (μm)	Δy_f, Δy_c (μm)	Δz (μm)	Δt (μs)
1	1.1	0.7	20	10	20	10, 20	20	5
2	1.2	0.8	25	10	20	$\leqslant$ 10, 20	20	5
3	1.2	0.8	20.7	10.35	20	20, 40	20	5
4	2.1	2.1	22	15	50	50,–	50	10

TABLE 2. Spatio-temporal discretization and domain dimensions for our DNS of cases 1–4.

Source	Case	Re^{tgt}	Ka	We	Fr	f^{tgt} (Hz)	Λ_x (mm)	Λ_z (mm)
Park & Nosoko (2003)	1	40.8	3923	11.8	3.7	19.1	20	20
Park & Nosoko (2003)	2	59.3	3923	6.3	4.4	17.0	25	20
Dietze *et al.* (2009)	3	15.0	509.5	8.0	2.2	16.0	20.7	20.7
This work	4	6.2	17.8	1.1	1.4	16.6	22.0	30.0

TABLE 3. Targeted flow conditions for our three-dimensional DNS of falling liquid films.

imposes a compression velocity normal to the interface (Rusche 2002). The contribution of capillary forces to the normal interfacial dynamic coupling condition (2.2) (there is no contribution to the tangential stress balance, as we assume $\sigma = \text{const.}$) is accounted for by the source term $F'''_{\sigma i}$ in (3.1*a*),

$$F'''_{\sigma i} = \sigma \hat{\kappa} \partial_{x_i} \alpha, \quad \hat{\kappa} = -\partial_{x_i} \hat{n}_i, \tag{3.3}$$

where $\hat{\kappa}$ and $\hat{n}_i$ denote the numerical estimates of interfacial curvature and normal vector to the interface, the latter being computed from the volume fraction field

$$\hat{n}_i = \partial_{x_i} \alpha / [\partial_{x_j} \alpha \partial_{x_j} \alpha]^{0.5}. \tag{3.4}$$

Table 2 lists the geometrical dimensions of the computational domain as well as the spatial and temporal discretization increments (we use a structured fixed grid of cuboid cells) employed for the three-dimensional simulations of cases 1 to 4. These were checked for grid independence with preliminary two-dimensional trial simulations. In the crosswise (y) direction, the domain is decomposed into a fine region (index f) of height H_f, containing the liquid phase and the free surface, and a coarser region (index c) for $H_f < y \leqslant H$, containing only gas. Our DNS were performed on the Juropa supercomputer at Forschungszentrum Jülich in the context of grant number HAC27. Simulation runs were typically performed on 1024 processors, requiring approximately 10 h for the calculation of one period (for the most expensive calculation, i.e. case 2).

4. Simulated cases and experimental validation

We start by further detailing the four considered cases of vertically falling liquid films introduced in the introduction. These are quantified in tables 4 and 3 in terms of flow conditions and fluid properties. We point out that an alternative parameter to the Reynolds number is the ratio $Re/Ka^{3/11}$, which appears naturally as the sole external control parameter in the boundary layer equations of two-dimensional film flow (Trifonov 2012) and takes the values 4.3, 6.2, 2.74 and 2.72 for cases 1 to 4, respectively.

https://doi.org/10.1017/jfm.2013.679 Published online by Cambridge University Press

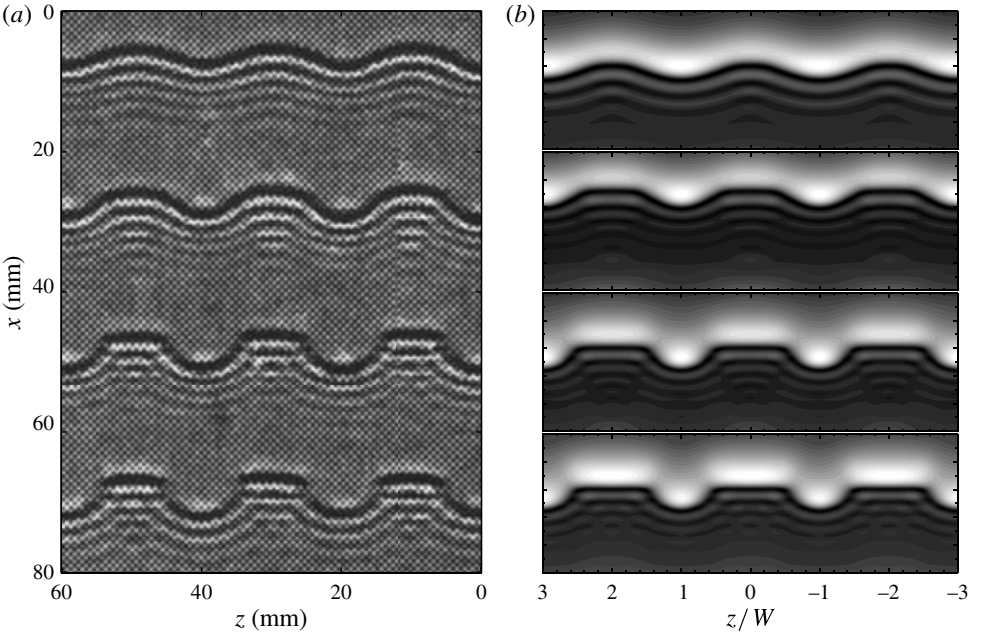


FIGURE 2. Case 1: $Re^{tgt} = 40.8$, $f^{tgt} = 19.1$ Hz. Comparison of numerical film thickness contours (*b*) with shadowgraph (*a*) obtained by Park & Nosoko (2003) (figure 7*c* therein; reproduced here with permission from John Wiley & Sons, Inc.).

Fluids	Case	ν (m^2 s^{-1})	ρ (kg m^{-3})	σ (N m^{-1})
Water	1, 2	0.893×10^{-6}	997.07	0.07201
DMSO/water	3	2.85×10^{-6}	1098.3	0.0484
DMS-T12	4	20.30×10^{-6}	949.0	0.020
Gas	1–4	15.58×10^{-6}	1.185	—

TABLE 4. Fluid properties for the investigated falling liquid films. DMSO, dimethylsulphoxide; DMS, dimethylsiloxane (silicone oil).

Cases 1 and 2 correspond to experimental investigations by Park & Nosoko (2003) performed with water as working liquid (fluid properties were evaluated at $T = 25\,^{\circ}$C). The Kapitza number for water is very high and, consequently, capillary forces and capillary waves play an important role. Figures 2 and 3 reproduce experimental shadowgraphs of the wave topology from Park & Nosoko (2003) in comparison with our DNS. The different representations of simulated wave fronts correspond to subsequent periods, while the experimental shadowgraphs show the spatial wave evolution. Our DNS capture the evolution of these experimental waves accurately. In both cases, wave fronts consist of horseshoe-shaped humps separated by more or less horizontal segments and preceded by a large number of capillary ripples organized in a complex interference pattern. Agreement between numerical and experimental data is reasonable, all the main features being captured by the simulations. However, there are two discrepancies. First, the width of the horizontal wave portions is overestimated by the DNS; and second, the last wave train in figure 3(*b*) shows the appearance of

https://doi.org/10.1017/jfm.2013.679 Published online by Cambridge University Press

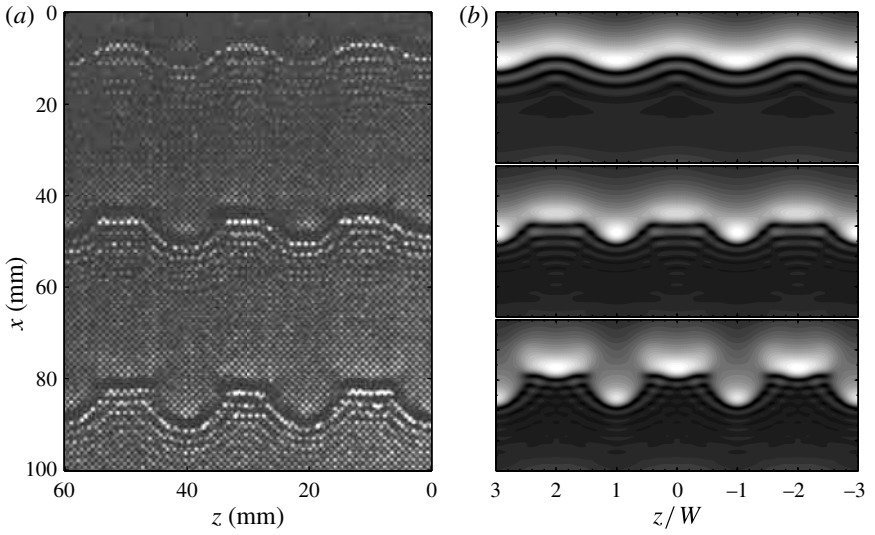


FIGURE 3. Case 2: $Re^{tgt} = 59.3$, $f^{tgt} = 17$ Hz. Comparison of numerical film thickness contours (*b*) with shadowgraph (*a*) obtained by Park & Nosoko (2003) (figure 7*d* therein; reproduced here with permission from John Wiley & Sons, Inc.).

a small V-shaped indentation there that is not observed in the experiments. These discrepancies could be due to imposing a constant value for the spanwise wavelength Λ_z in the simulations, whereas, in the experiments, slight changes in Λ_z may occur as the waves travel downstream. Alternatively, they could be due to the existence of sidewalls in the experiment, which may affect the distribution of wave segments within the given space. With regard to the V-shaped indentation, we point out that such a shape is visible in a single instance in the bottom right corner of figure 7(e) in Park & Nosoko (2003), although for a different Reynolds number.

Case 3 is extrapolated from *two-dimensional* flow conditions experimentally investigated by Dietze *et al.* (2009). In this case, $Ka = 509.5$ and the wave frequency and Reynolds number correspond to the experimentally controlled values. For our *three-dimensional* simulation, a spanwise wavelength $\Lambda_z = \Lambda_x = 20.7$ mm was additionally imposed. In the absence of three-dimensional experimental data for this case, figure 4 compares (two-dimensional) film thickness and streamwise velocity measurements from Dietze *et al.* (2009) with an 'equivalent' two-dimensional simulation of case 3: $Re^{\infty}_{DNS} = 15$, $f^{\infty}_{DNS} = 16$ Hz, $\Delta x = 20$ μm, $\Delta y = 10$ μm, $\Delta t = 5$ μs, where the superscript ∞ refers to the saturated state of surface waves achieved in the two-dimensional simulation.

Finally, case 4 corresponds to an experiment performed in the same test set-up as Rohlfs *et al.* (2012), using silicone oil as working liquid. Owing to the very low Kapitza number for this case, viscous forces are expected to dominate capillary forces and capillary waves to play a minor role. Figure 5 compares our DNS data for this case with a photograph as well as film thickness data measured with a confocal chromatic imaging technique. Overall agreement is again reasonable, as the DNS accurately reproduces the main features of the experimental data. A more detailed analysis shows that the same discrepancies observed in figure 3 also apply to case 4. The width of the horizontal wave segments is now slightly underestimated

https://doi.org/10.1017/jfm.2013.679 Published online by Cambridge University Press

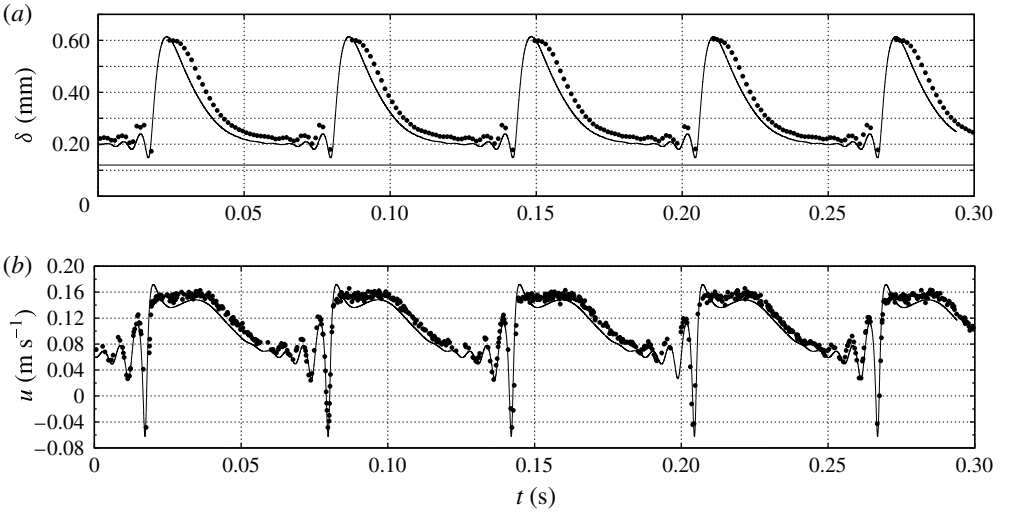


FIGURE 4. Case 3: Comparison of 'equivalent' two-dimensional numerical simulation ($Re^{\infty}_{DNS} = 15$, $Ka = 509.5$, $f^{\infty}_{DNS} = 16$ Hz, $\Delta x = 20$ μm, $\Delta y = 10$ μm, $\Delta t = 5$ μs) with time traces measured by Dietze *et al.* (2009): (*a*) film thickness (horizontal line indicates evaluation position for velocity data) and (*b*) streamwise velocity ($y = 120$ μm).

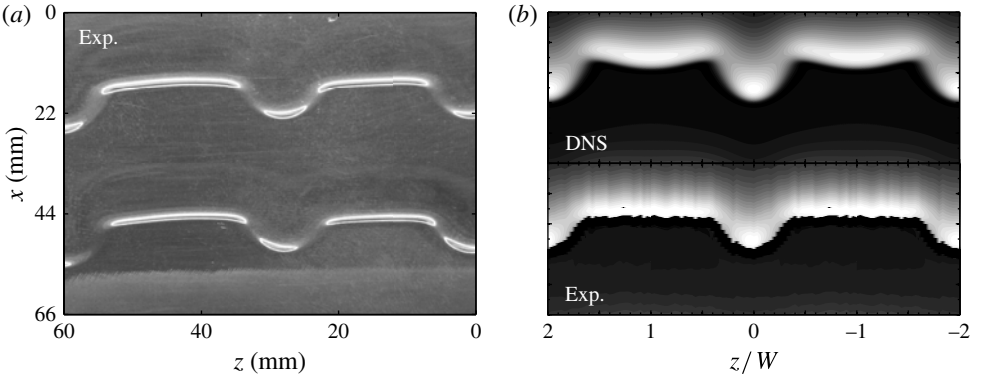


FIGURE 5. Case 4: $Re^{tgt} = 6$, $f^{tgt} = 17$ Hz. Comparison of numerical film thickness contours (*b*, top, $t = 0.28$ s) with experiments performed in the same test set-up as Rohlfs *et al.* (2012). (*a*) Photograph; (*b*, bottom) film thickness measurement data captured with a confocal chromatic imaging (CCI) technique (Cohen-Sabban, Gaillard-Groleas & Crepin 2001). Film thickness contours are normalized between extremal values.

by the DNS and they are once again indented downwards. We note that the window of visibility of the experiments for this case is restricted to two wave fronts far downstream of the inlet and, consequently, it is not known what time point from the DNS is most suitable for comparison. We have elected to represent the last time point of our DNS ($t = 0.28$ s), although better agreement is observed at earlier times, showing a less pronounced indentation of the horizontal wave segment (compare panels (*e*) and (*f*) in figure 9, which will be introduced later).

https://doi.org/10.1017/jfm.2013.679 Published online by Cambridge University Press

For cases 1, 2 and 4, the spanwise wavelength Λ_z in the simulations corresponds to the distance between needles immersed into the liquid film to excite three-dimensional surface waves in the experiments. Meanwhile, the streamwise wavelength Λ_x was measured from the respective shadow- and photographs for these cases (see figures 2*a*, 3*a* and 5*a*, respectively).

5. Results and discussion

The ensuing discussion of simulation data for cases 1 to 4 is structured in three parts. In the first part, § 5.1, we introduce the wave dynamics of the considered liquid films by analysing the time evolution of the three-dimensional free-surface topology. Therein, our DNS are complemented by long-time simulations with the WRIBL model of Scheid *et al.* (2006), which is validated in the Appendix. The second and main part, § 5.2, deals with the velocity field in the liquid film, dissecting flow structures within different regions of the three-dimensional surface waves and studying their effect on wave dynamics. In the third part, § 5.3, we explain the governing mechanism for the oscillating wave dynamics observed in § 5.1.

5.1. *Free-surface topology*

Figures 6–8 show the liquid film's free-surface evolution for cases 1 to 3 (case 4 will be discussed separately) as obtained from our DNS (a more vivid representation is provided in in the supplementary movies Case1_DNS to Case4_DNS, available at http://dx.doi.org/10.1017/ jfm.2013.679). We will refer to different panels of these figures as we discuss different stages of wave development. Additionally, figure 10 depicts time traces of several wave properties that have proven useful in the analysis of the wave dynamics. In all DNS, the initial film thickness perturbation consists of a large-amplitude cosinusoidal variation in streamwise direction (20% of mean thickness) onto which a small-amplitude spanwise variation (5% of mean thickness and also cosinusoidal) is superimposed. As a consequence, a predominantly two-dimensional large wave hump preceded by a growing number of capillary ripples develops in the early stages, as shown in panels (*a*,*b*) of figures 6–8. The amplitude of this hump, denoted $\hat{\delta}$, at first increases exponentially for all cases (showing that, although the initial perturbation was chosen rather large, the initial stage of wave growth is still governed by linear dynamics) and then decreases gradually as shown in figure 10(*b*). We have checked that the transition between these two evolution stages is associated with the saturation of the amplitude of the first capillary wave (roughly corresponding to panel (*a*) in figures 6–8).

The shape of the large hump in panels (*a*,*b*) is distorted in the spanwise direction, with a *trailing hump* in the central part preceded by *leading humps* in the outer portions, both reminiscent of the initial solution for which the thickness is smaller in the central part (and consequently the celerity too). The precursory capillary ripples emulate this shape. This wave packet subsequently evolves into a pronounced three-dimensional structure as the streamwise separation Δ between trailing and leading humps increases, attaining a maximum in panels (*e*) (roughly after 3–4 periods). The latter observation is more clearly evident in figure 10(*a*), representing time traces of Δ. In the first stage of this sequence (panels *c*), saddle points, arranged in a triangular pattern, appear on the main and capillary wave fronts. Between these saddle points, wave humps remain almost horizontal and are shaped like table-top hills. In the next stage (panels *d* to *e*), the leading horseshoe-shaped humps increasingly

https://doi.org/10.1017/jfm.2013.679 Published online by Cambridge University Press

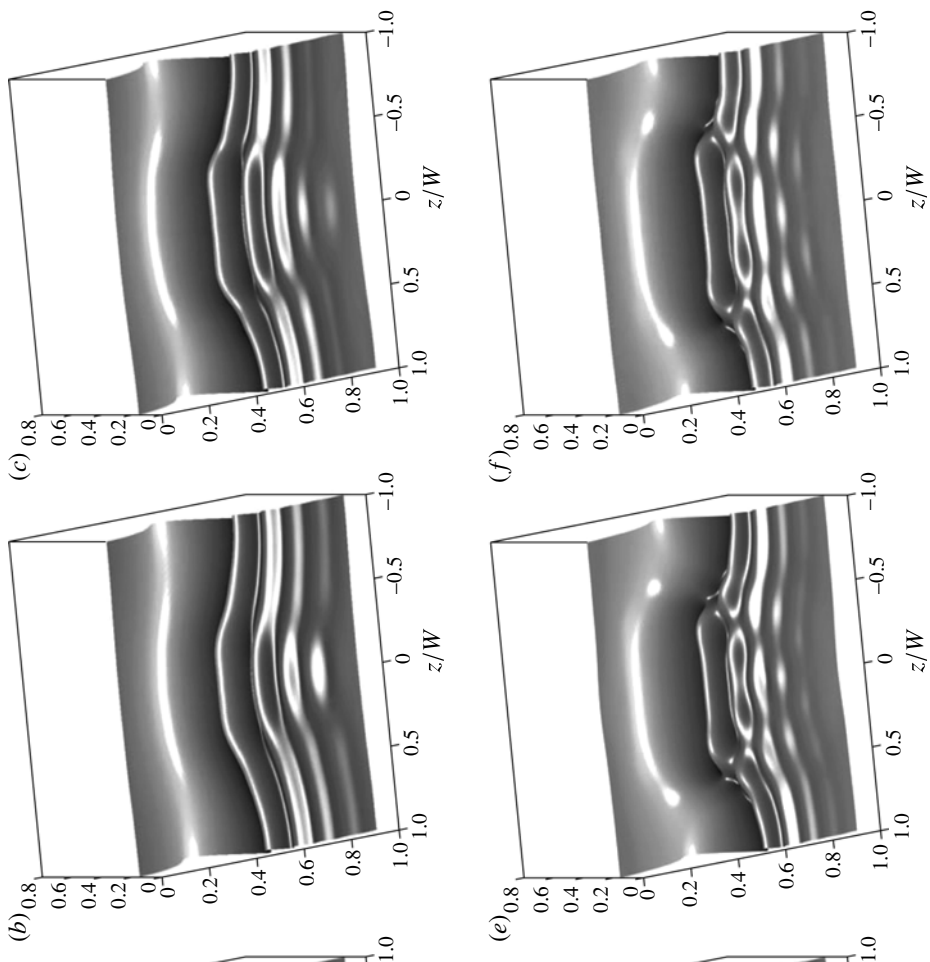


FIGURE 6. Case 1 (DNS): $Re^{fgt} = 41$, $f^{fgt} = 19$ Hz, $Ka = 3923$, $L = 20$ mm, $W = 10$ mm. Time evolution of liquid–gas interface: (*a*) $t = 0.075$ s; (*b*) $t = 0.10$ s; (*c*) $t = 0.125$ s; (*d*) $t = 0.18$ s; (*e*) $t = 0.2$ s; and (*f*) $t = 0.25$ s.

https://doi.org/10.1017/jfm.2013.679 Published online by Cambridge University Press

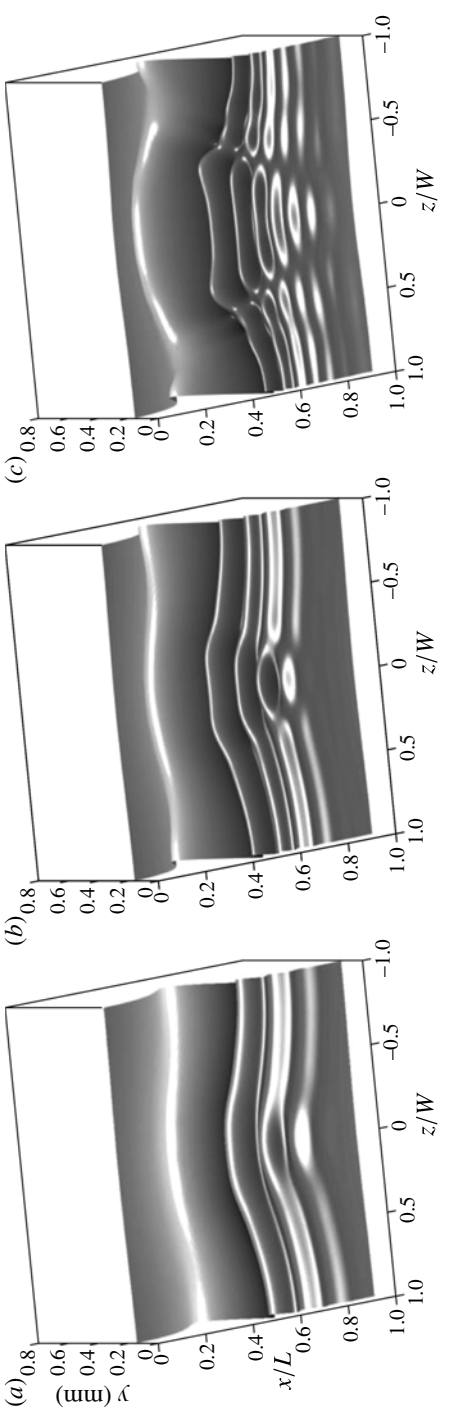


FIGURE 7. Case 2 (DNS): $Re^{tgt} = 59$, $f^{tgt} = 17$ Hz, $Ka = 3923$, $L = 25$ mm, $W = 10$ mm. Time evolution of liquid–gas interface: (*a*) $t = 0.05$ s; (*b*) $t = 0.075$ s; (*c*) $t = 0.125$ s; (*d*) $t = 0.14$ s; (*e*) $t = 0.175$ s; and (*f*) $t = 0.235$ s.

https://doi.org/10.1017/jfm.2013.679 Published online by Cambridge University Press

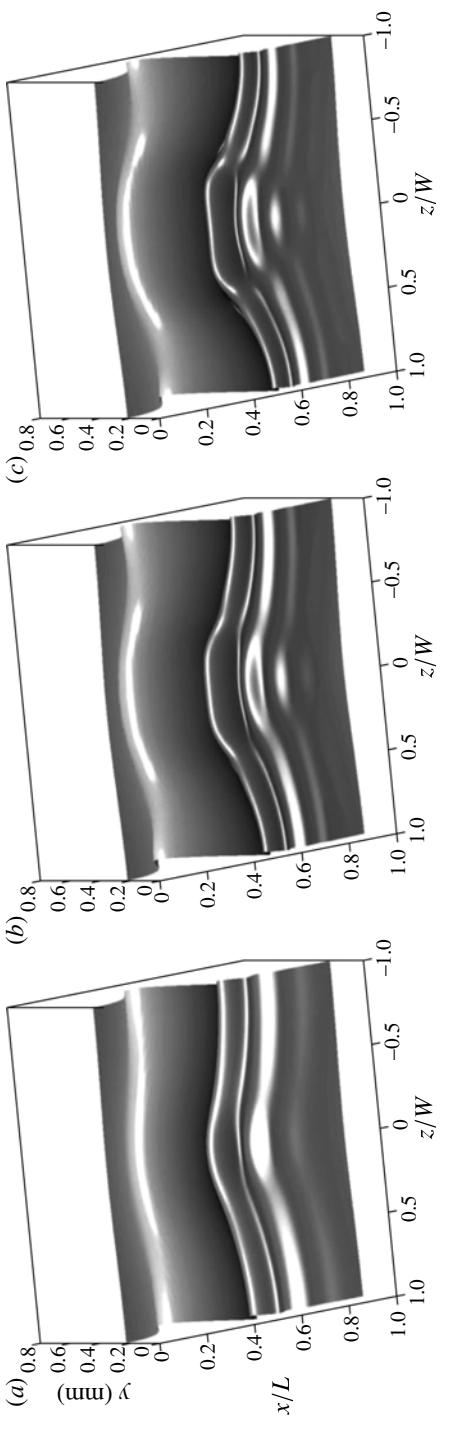


FIGURE 8. Case 3 (DNS): $Re^{fgt} = 15$, $f^{fgt} = 16$ Hz, $Ka = 509.5$, $L = 20.7$ mm, $W = 10.35$ mm. Time evolution of liquid–gas interface: (*a*) $t = 0.095$ s; (*b*) $t = 0.16$ s; (*c*) $t = 0.19$ s; (*d*) $t = 0.23$ s; (*e*) $t = 0.285$ s; and (*f*) $t = 0.30$ s.

https://doi.org/10.1017/jfm.2013.679 Published online by Cambridge University Press

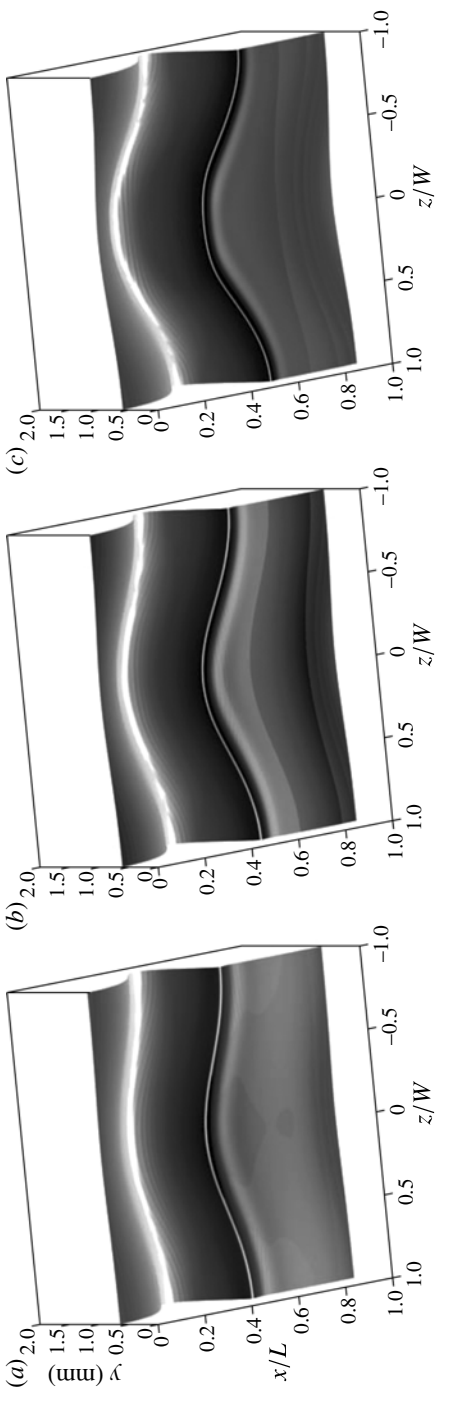


FIGURE 9. Case 4 (DNS): $Re^{lgt} = 6$, $f^{lgt} = 17$ Hz, $Ka = 17.8$, $L = 22$ mm, $W = 15$ mm. Time evolution of liquid–gas interface: (*a*) $t = 0.09$ s; (*b*) $t = 0.12$ s; (*c*) $t = 0.16$ s; (*d*) $t = 0.19$ s; (*e*) $t = 0.23$ s; and (*f*) $t = 0.28$ s.

https://doi.org/10.1017/jfm.2013.679 Published online by Cambridge University Press

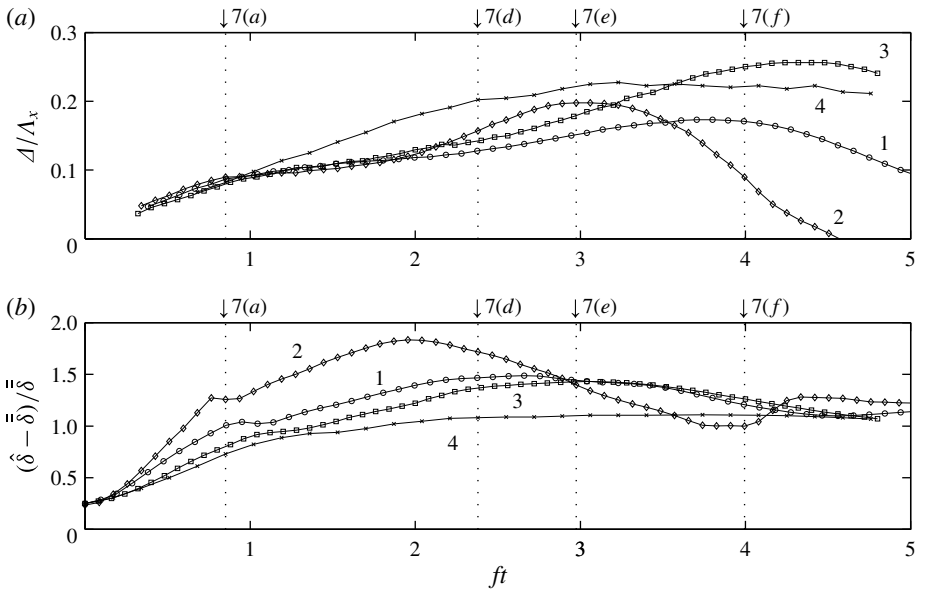


FIGURE 10. DNS time traces of wave kinematics: (*a*) streamwise distance Δ between leading and trailing humps; and (*b*) amplitude $\hat{\delta}$ of leading hump. Symbols: ○, case 1; ◇, case 2; □, case 3; ×, case 4. Arrows refer to characteristic time points for case 2, i.e. the various panels in figure 7. The first data points in panel (*a*) have been omitted due to problems in detection of the early-stage trailing hump. Abscissae are rescaled to units of the respective wave periods.

enclose the capillary wave region downstream of the trailing hump. For cases 2 and 3 (for case 1, this is less evident), the first capillary wave (the one closest to the trailing hump) thereby separates into a horizontal part that bridges the large leading humps, and arc-shaped outer parts that reconnect to the horizontal portion of the second capillary wave. In the process, the large leading humps broaden and decrease in amplitude (see amplitude time trace in figure 10*b*), while the bridging capillary ripples develop increasingly pronounced spanwise humps and swell at their extremities.

The last stage of wave dynamics simulated with our DNS (panels *e*,*f*) reveals a surprising feature first observed numerically by Kalliadasis *et al.* (2012) and experimentally by Alekseenko *et al.* (2012). Indeed, after having attained a maximal streamwise separation between leading and trailing humps in panels (*e*), cases 1 and 2 (we will show that this also occurs for cases 3 and 4) revert back to a more two-dimensional main hump shown in panels (*f*). Thereby, leading humps slow down with respect to the trailing hump (see Δ plot in figure 10*a*), while contracting in the spanwise direction and thus widening the bridging capillary humps. The instantaneous Reynolds number, evaluated according to (2.8) and plotted in figure 11 as a function of time, attains a maximum at the onset of this stage (maximal values for each case are listed in table 1 as Re^{max}_{DNS}).

Compression and expansion of the bridging capillary waves shows the ability of the three-dimensional structures to oscillate. We will explain the governing mechanism for the observed transition from three-dimensional to more two-dimensional waves in § 5.3, after all the relevant features of the flow and wave dynamics have been

https://doi.org/10.1017/jfm.2013.679 Published online by Cambridge University Press

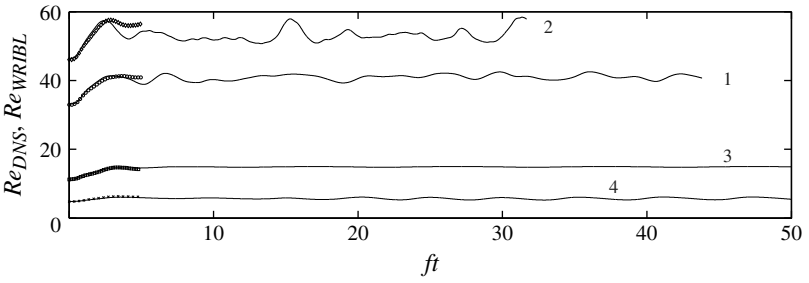


FIGURE 11. Transition to oscillating wave dynamics. Time traces of instantaneous Reynolds number evaluated according to equation (2.8) for DNS (symbols, short-time simulations) and WRIBL (solid lines, long-time simulations) data, respectively. Symbols: ○, case 1; ◇, case 2; □, case 3; ×, case 4. Maximal values of Re_{DNS} are reported as Re_{DNS}^{max} in table 1.

introduced. For the time being, it is appealing to consider the long-time fate of three-dimensional wave structures. Owing to the extremely high computational cost, this was not feasible with DNS. Instead, long-time simulations were performed with the low-dimensional WRIBL model of Scheid *et al.* (2006). The predictions of this model are scrutinized against the background of our DNS in the Appendix, and movies of WRIBL simulations are also available (see supplementary movies Case1_WRIBL–Case4_WRIBL).

To solve the WRIBL model (see equation (6.2) in Scheid *et al.* (2006) for film thickness h as well as streamwise and spanwise flow rates q_x and q_z), a pseudospectral scheme with the spatial derivatives evaluated in Fourier space and the nonlinearities in real space has been employed. The time dependence is accounted for by a fifth-order Runge–Kutta scheme, which allows control of truncation errors by the difference with an embedded fourth-order scheme (Press *et al.* 1992). The time step was thus dynamically adapted in order to limit this truncation error on each variable (h, q_x and q_z) to $\leqslant 10^{-4}$. Aliasing has been treated by using the 'two-thirds' rule that applies for quadratically nonlinear equations (as for the Navier–Stokes equations) (Boyd 2001), even though the order of nonlinearity of the WRIBL equation system is much larger than two (seven for the regularized model of Scheid *et al.* (2006) used here). However, keeping the first two-thirds of the Fourier modes in each direction and before each iteration was enough to reach convergence, which was verified by doubling the mesh points in each direction and observing no qualitative difference in the patterns obtained. Therefore, 256×256 modes (i.e. 512×512 grid points) were necessary to simulate cases 1 and 2, while only 128×128 modes (i.e. 256×256 grid points) were necessary for cases 3 and 4.

Long-time WRIBL simulation results are displayed in figures 11 and 12. Figure 11 superimposes the Reynolds number (according to (2.8)) time traces obtained from the WRIBL simulations onto those of the DNS and shows first indications of long-term oscillatory dynamics. The onset of these is just captured by our short-time DNS, and agreement between DNS and WRIBL data is fair (qualitative, if not quantitative, for all cases). To make the transitions between two- and three-dimensional wave topology during these oscillations more apparent, we introduce the streamwise and spanwise surface deformation energies of the film thickness field (Joo & Davis 1992,

https://doi.org/10.1017/jfm.2013.679 Published online by Cambridge University Press

Scheid *et al.* 2008*a*,*b*):

$$E_x(t) = \frac{1}{N_x N_z} \sum_{j=1}^{N_z} \left[\sum_{m=1}^{N_x/2-1} |A_m(z_j, t)|^2 \right]^{1/2},$$

$$A_m(z, t) = \sum_{l=0}^{N_x-1} \delta(x_l, z, t) \exp\left[\frac{\mathrm{i}2\pi ml}{N_x} \right], \tag{5.1a}$$

$$E_z(t) = \frac{1}{N_x N_z} \sum_{l=1}^{N_x} \left[\sum_{n=1}^{N_z/2-1} |B_n(x_l, t)|^2 \right]^{1/2},$$

$$B_n(x, t) = \sum_{j=0}^{N_z-1} \delta(x, z_j, t) \exp\left[\frac{\mathrm{i}2\pi nj}{N_z} \right]. \tag{5.1b}$$

Figure 12 plots time traces of E_x and E_z (non-dimensionalized with $\bar{\bar{\delta}}$) for cases 1 to 4, as obtained from the WRIBL model. The abscissa represents the product of time and frequency, showing that up to 50 periods are considered. As suggested by our short-term DNS (approximately five periods), oscillations between a pronounced three-dimensional (large E_z, low E_x) and a more two-dimensional (low E_z, large E_x) free-surface topology occur for all cases, confirming first observations by Kalliadasis *et al.* (2012). The frequency of these oscillations is between 5 and 10 times smaller than the wave frequency. Although all cases oscillate, they evince a number of subtle differences. For case 3, for example, phase opposition between E_x and E_z is evident, while the Reynolds number, evaluated according to (2.8) and plotted in figure 11, remains more or less constant. In this case, energy is thus exchanged between two- and three-dimensional surface structures.

For case 4, a more detailed analysis is necessary. The time traces in figures 11 and 12(*d*) evince two separate stages. In the first (up to roughly 15 periods), low-amplitude oscillations of E_x and E_z occur, while the Reynolds number remains more or less constant. Here, the streamwise separation of leading and trailing humps oscillates back and forth (see WRIBL supplementary movie Case4_WRIBL for case 4). In the second stage (from 15 to 50 periods), the Reynolds number starts to oscillate and the amplitude of the deformation energy oscillation increases significantly. This is caused by the leading humps protruding so far downstream that the spanwise coherence of the wave front is ruptured. From then on, oscillations of E_x and E_z are caused by the leading humps repeatedly overtaking the trailing humps (see supplementary movie Case4_WRIBL). As opposed to case 3, time traces for the deformation energies are not significantly out of phase. Here, energy remains mainly trapped within the respective structures, and oscillations are of a global nature.

For cases 1 and 2, characterized by large Re and Ka values, oscillations are far more irregular. For the lower Reynolds number, E_x and E_z are almost in phase opposition, as was observed for case 3, while for case 2 both signals are close to being in phase, as was observed for case 4. Thereby, for the more 'in-phase scenario' (cases 2 and 4), the levels of E_x and E_z are similar, while there is a significant separation between the two for cases 1 and 3, where deformations due to spanwise modulations dominate ($E_z > E_x$).

To complete our discussion of wave dynamics, we discuss the DNS results for case 4 in figure 9, having mainly concentrated on cases 1 to 3 up until now. These

https://doi.org/10.1017/jfm.2013.679 Published online by Cambridge University Press

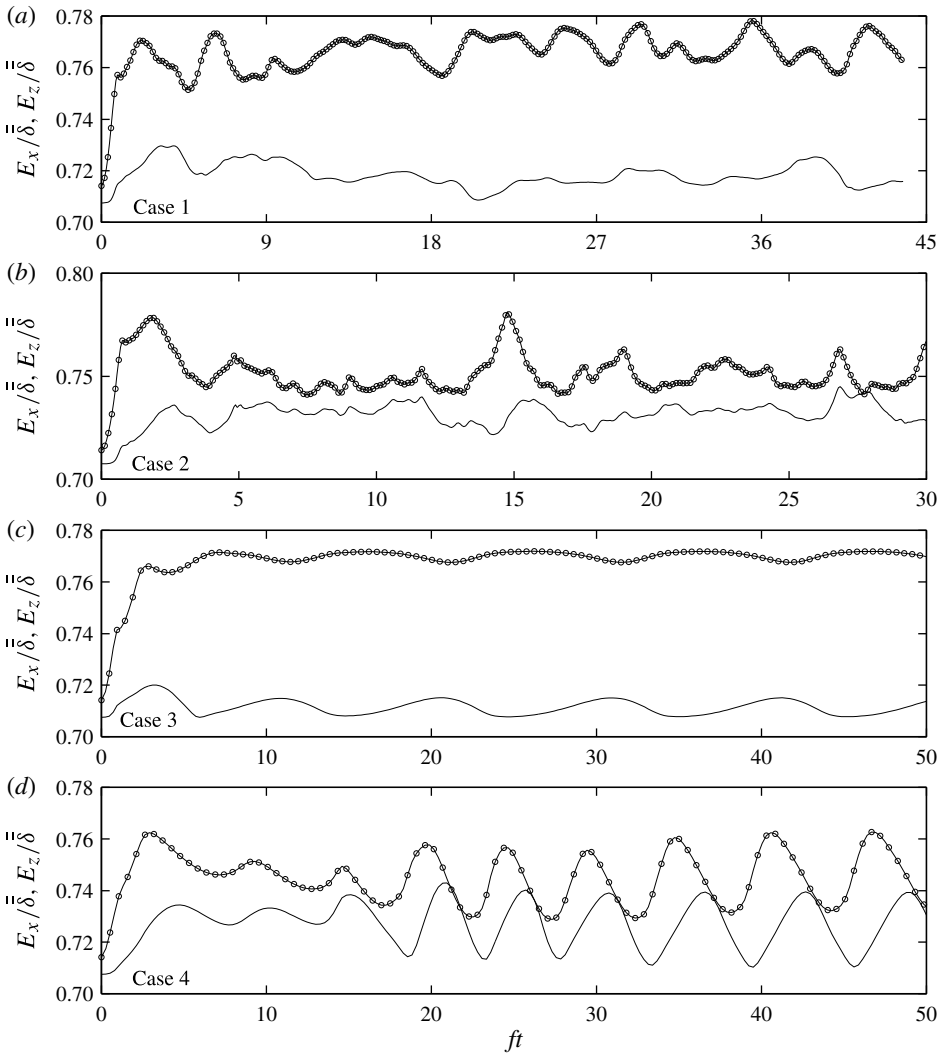


FIGURE 12. Long-time WRIBL simulations showing oscillating wave dynamics for (*a–d*) cases 1 to 4, respectively. Plots show time traces of surface deformation energies E_x (symbols, $E_x/\bar{\bar{\delta}}$) and E_z (solid line, $E_z/\bar{\bar{\delta}}$) evaluated based on equations (5.1*a*) and (5.1*b*), quantifying film thickness variations in streamwise and spanwise directions.

cases are characterized by large values of the Kapitza number and consequently a large number of precursory capillary ripples, while, for case 4, *Ka* is smaller by two orders of magnitude. Consequently, among the dissipative mechanisms counteracting the source of the gravity-driven instability, viscous dissipation dominates surface-tension-based stabilization. The region preceding the large humps thus consists of a much thinner film developing very few capillary waves. This is evident when comparing figure 9 (DNS time evolution of surface waves for case 4) with figures 6–8. Indeed, panel (*f*) of figure 9 shows that, although the large hump topology is similar to that of cases 1 to 3, only a single small-amplitude capillary wave occurs, which is enslaved to the shape of the large hump. Nonetheless, this single capillary

https://doi.org/10.1017/jfm.2013.679 Published online by Cambridge University Press

wave suffices to initiate oscillating wave dynamics also for case 4, as was established above. We will demonstrate the role of capillary waves for such oscillations in § 5.3, which explains the governing mechanism of this phenomenon. Finally, a second effect of the Kapitza number needs to be considered. As a result of the small value of Ka for case 4, much larger-amplitude three-dimensional wave structures occur than for the other cases (see figure 13). We will see in § 5.3 that this effect, associated with the absence of pronounced capillary waves for case 4, enables the leading humps to protrude much further downstream, explaining the large changes in surface deformation energy observed in figure 12(*d*).

To conclude the current section, we point out that figures 6–9 evince a general observation that the liquid is segregated into regions of very small film thickness (residual film) and regions carrying the largest amount of mass (large wave humps). We will show in the next section that these respective regions are associated with significantly different flow dynamics.

5.2. *Velocity field*

Figure 13 represents maps of the inverse Weber number based on the local (hence the hat symbol) streamwise flow rate per unit width $q_{lx} = \int_0^\delta u\,\mathrm{d}y$ (2.8), i.e. $\hat{We}^{-1} = \rho q_{lx}^2/(\sigma\delta)$. These show that the liquid film's flow field is separated into two distinct regions: (i) an inertia-dominated region associated with the large wave humps, where $\hat{We}$ is small and the local Reynolds number $\hat{Re} = q_{lx}/\nu_l$ is of $O(\hat{Re}) = 100$ (300 for case 2; see figure caption); and (ii) a visco-capillary region dominated by capillary and/or viscous forces (the most relevant effect is determined by the Kapitza number), where $\hat{We}$ is large and $O(\hat{Re}) = 1$. This large separation of scales explains a number of previous observations in film flows. For instance, Ishigai *et al.* (1972) report falling liquid films to become intermittently turbulent at $O(Re) = 100$, which is low compared to single-phase flows. However, assuming that $\max(\hat{Re})$ within a wavy film is approximately five times larger than Re (the mean value), it thus attains values of the order of the critical Reynolds number for plane Poiseuille flow $O(650)$ when $Re = 75$. Further, Miya, Woodmanee & Hanratty (1971) observed a periodic relaminarization of the flow in their measurements of velocity time traces within the film, which can be explained by the intermittent passage of the low-Reynolds-number visco-capillary region at the measuring position.

Meanwhile, wall shear stress distributions in figure 14 show that regions (i) and (ii), as indicated in figure 13(*c*), are associated with distinctly different flow features. While in the visco-capillary region shear stress variations closely correlate with film thickness variations, the inertial region suggests quite complicated small-scale flow structures, although film thickness variations there occur on a large scale. In the following sections, we investigate these flow features in further detail by dissecting the velocity field into x–y, z–y and x–z slices at the various positions highlighted in figures 13 and 14. Accordingly, time points associated with these figures (unless otherwise mentioned) correspond to panels (*e*) and (*d*) in figures 6 and 7 (cases 1 and 2) and panels (*f*) in figures 8 and 9 (cases 3 and 4).

5.2.1. *The inertia-dominated region*

Figure 15 shows the velocity field for cases 1, 2 and 4 projected into z–y planes at the streamwise position of the leading hump (case 3 shows no qualitative difference

https://doi.org/10.1017/jfm.2013.679 Published online by Cambridge University Press

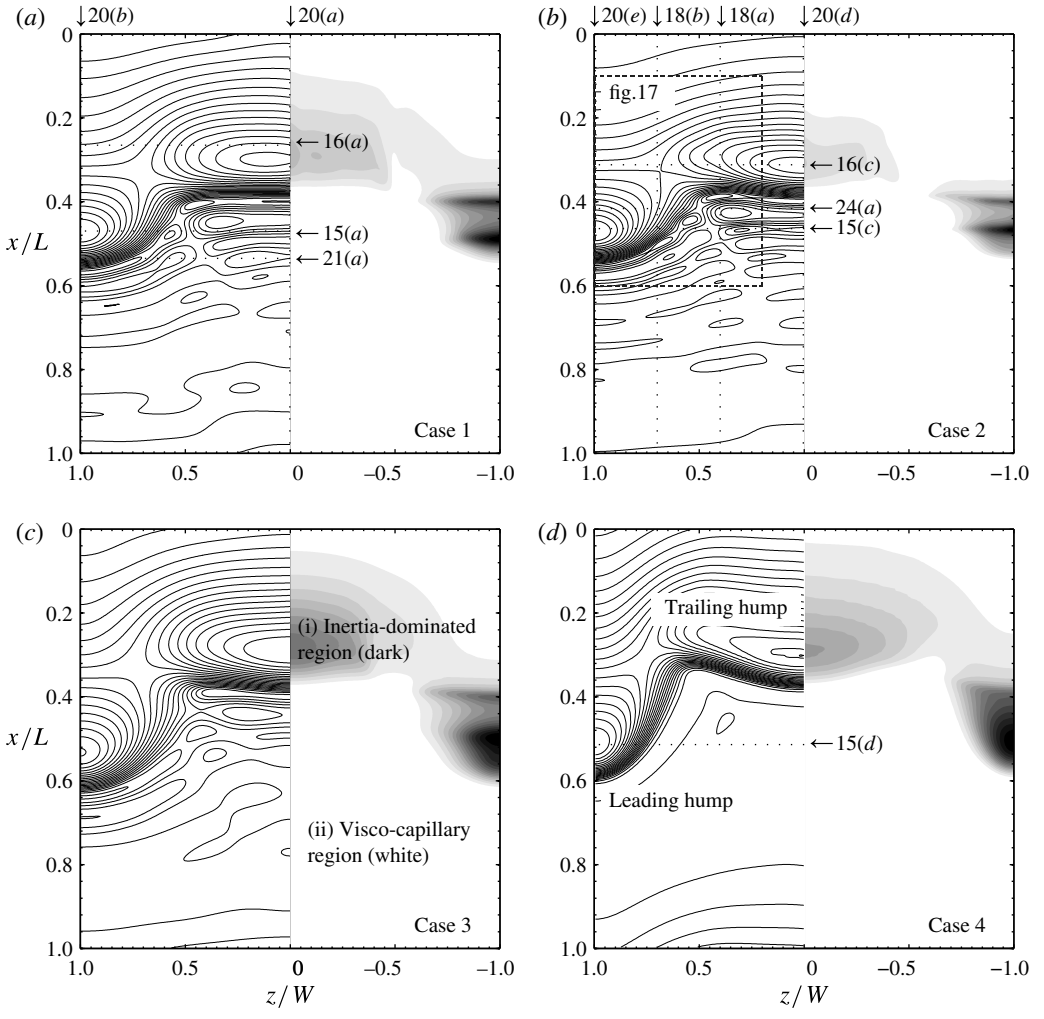


FIGURE 13. Contours of film thickness δ (left half-plane) and inverse local Weber number $1/\hat{We} = \rho q_{lx}^2/(\sigma\delta)$ (right half-plane) for: (*a*) case 1, $\delta \in [0.06, 0.45]$ mm, $1/\hat{We} \in [0.7, 0]$; (*b*) case 2, $\delta \in (0.06, 0.6)$ mm, $1/\hat{We} \in [1.7, 0]$; (*c*) case 3, $\delta \in (0.12, 0.64)$ mm, $1/\hat{We} \in [0.9, 0]$; and (*d*) case 4, $\delta \in (0.49, 1.7)$ mm, $1/\hat{We} \in [6.5, 0]$; corresponding to panels (*e*), (*d*), (*f*) and (*f*) in figures 6, 7, 8 and 9, respectively. Dotted lines and associated figure labels refer to velocity field slices plotted in §§ 5.2.1 and 5.2.2. Contour levels from white (minimum) to black (maximum) are uniformly distributed between extremal values. Maximal local Reynolds numbers $\hat{Re} = q_{lx}/\nu_l$ for panels (*a*) to (*d*) are 164, 300, 55 and 24, respectively. The box in panel (*b*) highlights the area of the view represented in figure 17.

and is not shown here), where a large vortex is seen to occur (the white contour line delimits regions where the streamwise flow velocity surpasses the wave celerity). This vortex remains unaltered in the wave-fixed reference frame, because the wave velocity has no spanwise component. Its occurrence follows simply from mass conservation. Considering a surface wave, its liquid–gas interface becomes a stream surface in the

https://doi.org/10.1017/jfm.2013.679 Published online by Cambridge University Press

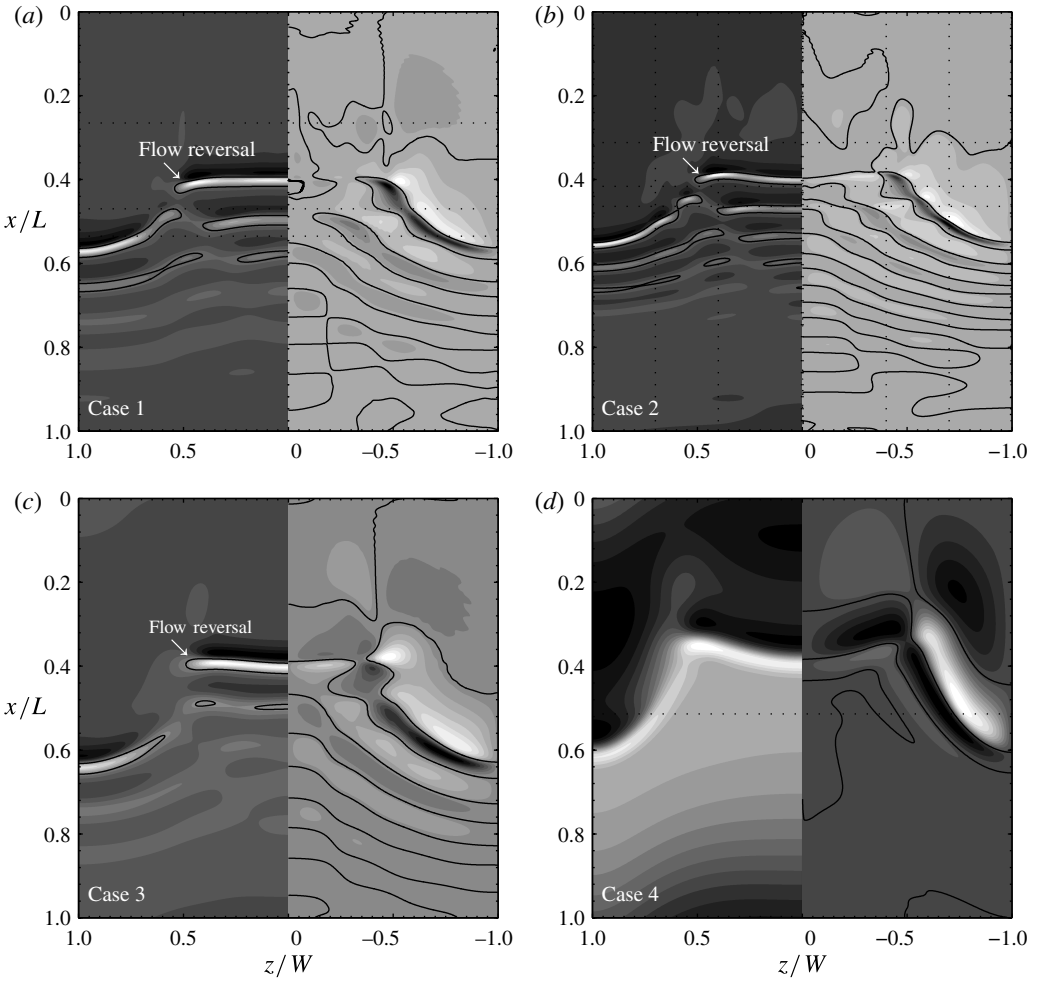


FIGURE 14. Contours of wall shear stress components $\tau_{wx} = -\mu_l \partial_y u|_{y=0}$ (left half-plane) and $\tau_{wz} = -\mu_l \partial_y w|_{y=0}$ (right half-plane) for: (*a*) case 1, $\tau_{wx} \in [-7, 9.9]$ Pa, $\tau_{wz} \in [-4, 2.2]$ Pa; (*b*) case 2, $\tau_{wx} \in [-7.7, 13.9]$ Pa, $\tau_{wz} \in [-8, 3.8]$ Pa; (*c*) case 3, $\tau_{wx} \in [-8.8, 8.1]$ Pa, $\tau_{wz} \in [-2.5, 2.1]$ Pa; and (*d*) case 4, $\tau_{wx} \in [-11, -2.5]$ Pa, $\tau_{wz} \in [-1.2, 2.9]$ Pa; at time points corresponding to figure 13. Dotted lines are identical to those in figure 13 in both position and purpose. Contour levels from black (minimum) to white (maximum) are uniformly distributed between extremal values (black line indicates zero value).

wave-fixed reference frame. This is because, at the interface,

$$\left.\begin{aligned} (\boldsymbol{v} - [c, 0, 0]) \cdot \boldsymbol{n} = \partial_t \delta + c\, \partial_x \delta = 0 \qquad \text{with} \\ \boldsymbol{v} = [u, v, w], \quad \boldsymbol{n} = \left[-\partial_x \delta, 1, -\partial_z \delta\right], \quad v = \partial_t \delta + u\, \partial_x \delta + w\, \partial_z \delta. \end{aligned}\right\} \tag{5.2}$$

The liquid within the film is thus confined between the free surface and the wall as well as the spanwise planes of symmetry. If spanwise flow exists within these segments, it must do so in the form of vortices with streamwise vorticity. As shown in figure 15(*c*), the driving force for the spanwise flow within the leading hump results

https://doi.org/10.1017/jfm.2013.679 Published online by Cambridge University Press

from a spanwise wall pressure gradient, $\partial_z p_w$, caused by a change in free-surface curvature between the large hump and the trough of the first capillary wave (through the effect of capillary forces). This mechanism is particularly effective in the spanwise direction, as it is not counteracted by gravity, and has recently been invoked by Georgantaki *et al.* (2011) to explain the stabilization of curved wave fronts spanning the width of laterally confined inclined film flows. It forces near-wall liquid from the hump to the capillary trough, thus driving the vortex. The associated transverse flow is strongest for cases 2 and 1 (owing to larger surface tension), while case 4 also displays spanwise velocity values of the same magnitude. Meanwhile, streamwise backflow occurs at the capillary trough for cases 1 and 2, which will be discussed further in § 5.2.2.

Quite different flow features occur within the trailing hump. Figure 14 shows that the wall shear stress components in this region change sign (indicated by black contour line) several times at a given streamwise position. For cases 1 and 2, exhibiting the largest local Reynolds number values, wall shear stress contours evince the most complicated flow patterns. This is confirmed by panels (*a*) and (*b*) in figure 16, showing z–y slices of the projected velocity field at the streamwise position of the trailing wave crest. It is clear from these representations that wall shear stress sign changes in figure 14 are associated with intricate flow structures carrying streamwise vorticity. These flow structures originate at the wall, as can be observed in supplementary movies Case1_DNS_TH and Case2_DNS_TH, showing the time evolution of the velocity field for cases 1 and 2 within the z–y slices represented in panels (*a*,*c*), i.e. for the constant relative streamwise positions $x/L = 0.27$ and $x/L = 0.31$ in the wave-fixed reference frame. After their inception at the wall, these structures grow until they cover the entire film thickness, upon which they interact with the free surface. For example, around the spanwise position $z/W = -0.55$ in panel (*c*), the flow is oriented normal to the free surface and produces an upwelling. Judging from the streamwise velocity contours, the flow is slower there and separates two large regions left and right (encompassed by the white contour line) where streamwise velocity surpasses wave celerity.

To analyse the origin of the vorticity-carrying structures in more detail, figure 16(*b*) shows the (normalized) spanwise wall pressure derivative corresponding to panels (*a*) and (*c*). Within the trailing hump, variations in film thickness are weak and consequently the pressure gradient is small. Clearly, it does not entirely govern the spanwise flow, as several changes in flow direction occur without corresponding sign changes in the pressure derivative. The vortical flow structures are thus affected by the three-dimensional nature of the flow as well as streamwise inertia, which plays a role due to the large maximal values of $\hat{Re}$ (150 and 300 for cases 1 and 2, respectively). These observations suggest a subtle destabilizing mechanism within the more or less two-dimensional trailing hump at high Reynolds number values. Owing to the absence of spanwise gravity, small perturbations of the free surface readily generate vorticity at the wall, where velocity is low and the flow is thus most sensitive. The resulting vorticity-carrying flow structures disturb the main flow, which, given enough inertia, will produce flow structures that are misaligned with the film thickness (and resulting pressure perturbations) and thus retro-act on them. This mechanism could play a role in the initiation and/or the selection of turbulent structures in falling liquid films at sufficiently large Reynolds number. Verification of this conjecture requires simulations at larger Re, which are outside the scope of this work. In the leading hump, owing to its distinctly three-dimensional horseshoe shape, there is already a large-scale three-dimensional flow, which is less easily disturbed

https://doi.org/10.1017/jfm.2013.679 Published online by Cambridge University Press

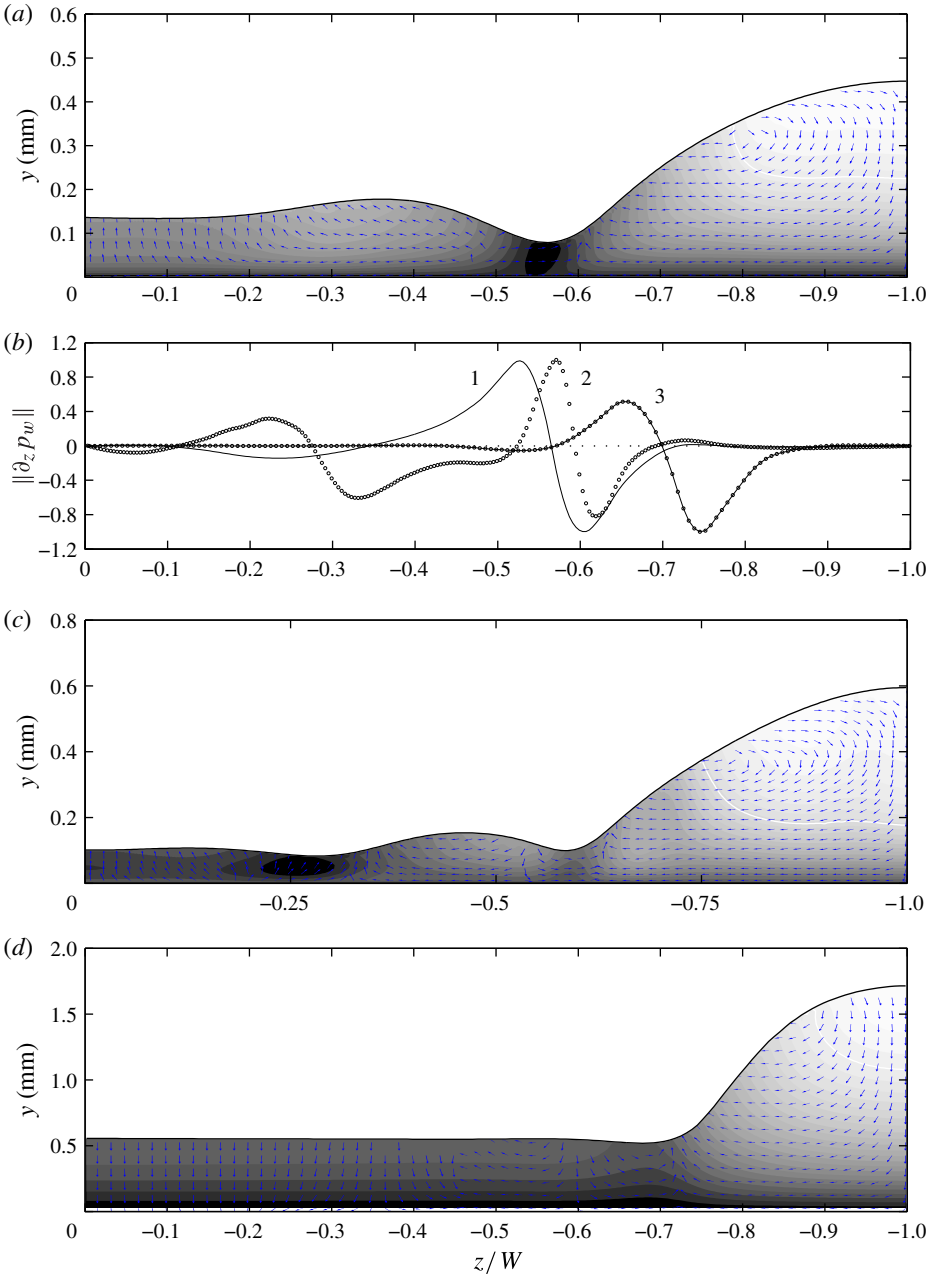


FIGURE 15. (Colour online) (*a*,*c*,*d*) Velocity field projections into z–y slices at streamwise positions of leading humps (see figures 13 and 14) and (*b*) wall pressure distribution (normalized with maximal magnitude): (*a*) case 1, $x/L = 0.47$ (black -0.02 m s^{-1}, white 0.44 m s^{-1}), $|w|_{max} = 0.08$ m s^{-1}; (*b*) solid line, case 1; circles, case 2; line with circles, case 4; (*c*) case 2, $x/L = 0.46$ (black -0.10 m s^{-1}, white 0.60 m s^{-1}), $|w|_{max} = 0.14$ m s^{-1}; and (*d*) case 4, $x/L = 0.51$ (black 0.005 m s^{-1}, white 0.42 m s^{-1}), $|w|_{max} = 0.07$ m s^{-1}. Arrows are normalized with their magnitude. Contours indicate streamwise velocity component (white contour line corresponds to wave celerity $c = f\Lambda_x$).

https://doi.org/10.1017/jfm.2013.679 Published online by Cambridge University Press

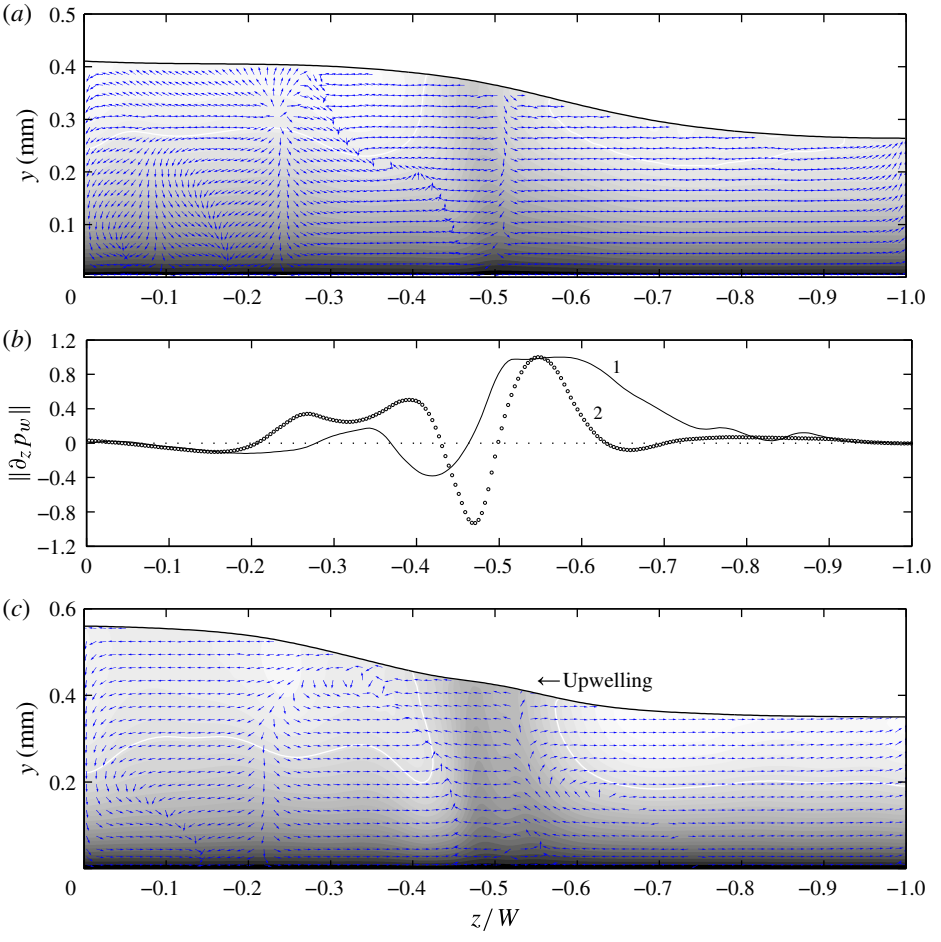


FIGURE 16. (Colour online) (*a*,*c*) Velocity field projection into z–y slices at streamwise position of trailing wave crest (see figures 13 and 14) and (*b*) wall pressure distribution (normalized with maximal magnitude): (*a*) case 1, $x/L = 0.27$ ($u_{min} = 0.003$ m s^{-1}, $u_{max} = 0.55$ m s^{-1}), $|w|_{max} = 0.09$ m s^{-1}; (*b*) solid line, case 1; circles, case 2; and (*c*) case 2, $x/L = 0.31$ ($u_{min} = 0.003$ m s^{-1}, $u_{max} = 0.55$ m s^{-1}), $|w|_{max} = 0.09$ m s^{-1}. Arrows are normalized with their magnitude. Contours (increasing from black to white) indicate streamwise velocity component (white line corresponds to wave celerity $c = f\,\Lambda_x$).

by small free-surface perturbations, so that the described mechanism is less effective than in the trailing hump, although the local Reynolds number is larger in the leading hump (albeit not drastically).

To obtain a top view of the three-dimensional flow features in the large wave humps, figure 17 shows the velocity field in the wave-fixed reference frame within x–z slices at two different wall distances for case 2. This representation evinces several vortices with crosswise (in y direction) vorticity. Two large co-rotating vortices are seen in the leading hump, which subdivide a larger circulation region there. This region persists over the entire height of the wave as shown in the x–y slice of figure 18(*b*). The centres of the co-rotating vortices move towards the trailing hump as the wall distance increases, disrupting a third vortex associated with the leading

https://doi.org/10.1017/jfm.2013.679 Published online by Cambridge University Press

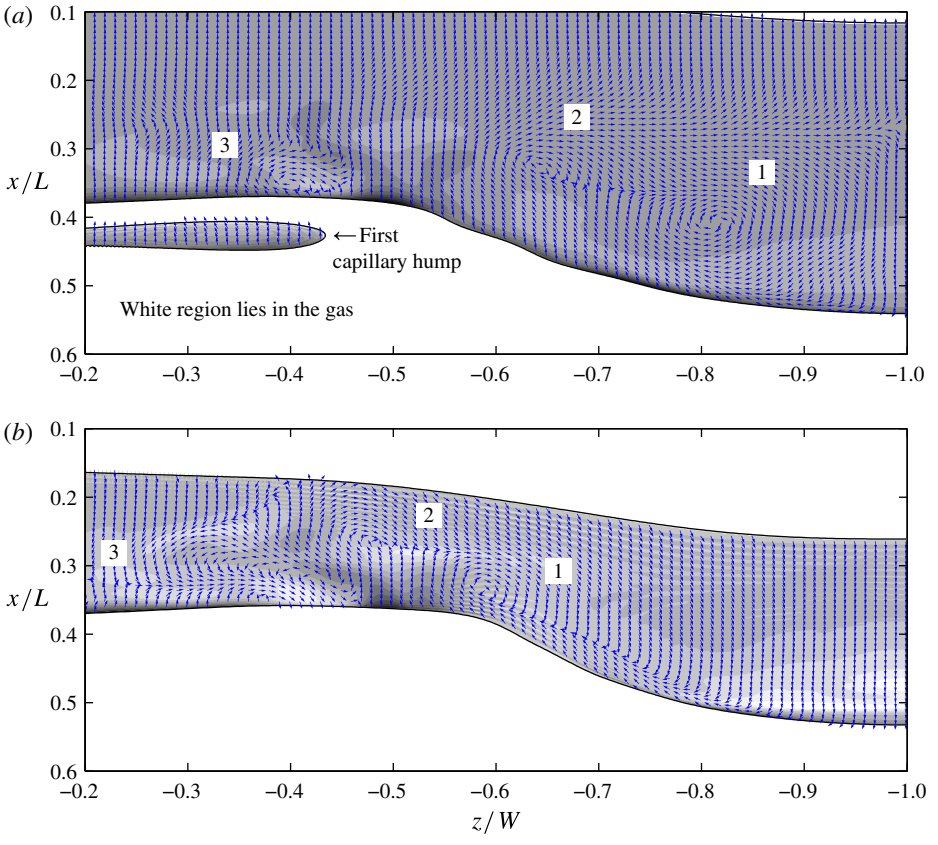


FIGURE 17. (Colour online) Case 2: velocity field projection into x–z slices (top view) at different wall distances within the large wave humps: (*a*) $y = 0.2$ mm (black $v = 0.003$ m s^{-1}, white $v = 0.55$ m s^{-1}), $|w|_{max} = 0.09$ m s^{-1}; and (*b*) $y = 0.3$ mm (black $v = 0.003$ m s^{-1}, white $v = 0.55$ m s^{-1}), $|w|_{max} = 0.09$ m s^{-1}. Velocity vectors are considered in the wave-fixed reference frame ($u \to u - c = u - f^{tgt}\Lambda_x$) and arrows are normalized with their magnitude. Contours (equidistantly valued) indicate crosswise velocity component.

front of the trailing hump and changing the sense of rotation of the flow there (from clockwise to anticlockwise). As a consequence, a stretched loop-shaped flow structure prevails almost across the entire width of the trailing hump. The associated spanwise velocities w are considerable, as shown in figure 18.

The flow structures identified in this section are relevant for heat and mass transfer operations, which typically involve falling liquid films (e.g. in distillation columns). Their three-dimensional nature explains why wave-induced intensification of heat and mass transfer has been found to be significantly more pronounced in three-dimensional than in two-dimensional films (Alekseenko *et al.* 1994). In addition to the obvious advantage of adding spanwise convective transport in a three-dimensional flow, spanwise flow structures, due to the absence of gravity in this direction, cover large regions of the main wave, displaying a more complicated range of length scales than their two-dimensional counterparts (Miyara 1999; Dietze, Leefken & Kneer 2008; Malamataris & Balakotaiah 2008). This complexity in part results from the relevance of inertia within the large wave humps, which we have shown to exhibit

https://doi.org/10.1017/jfm.2013.679 Published online by Cambridge University Press

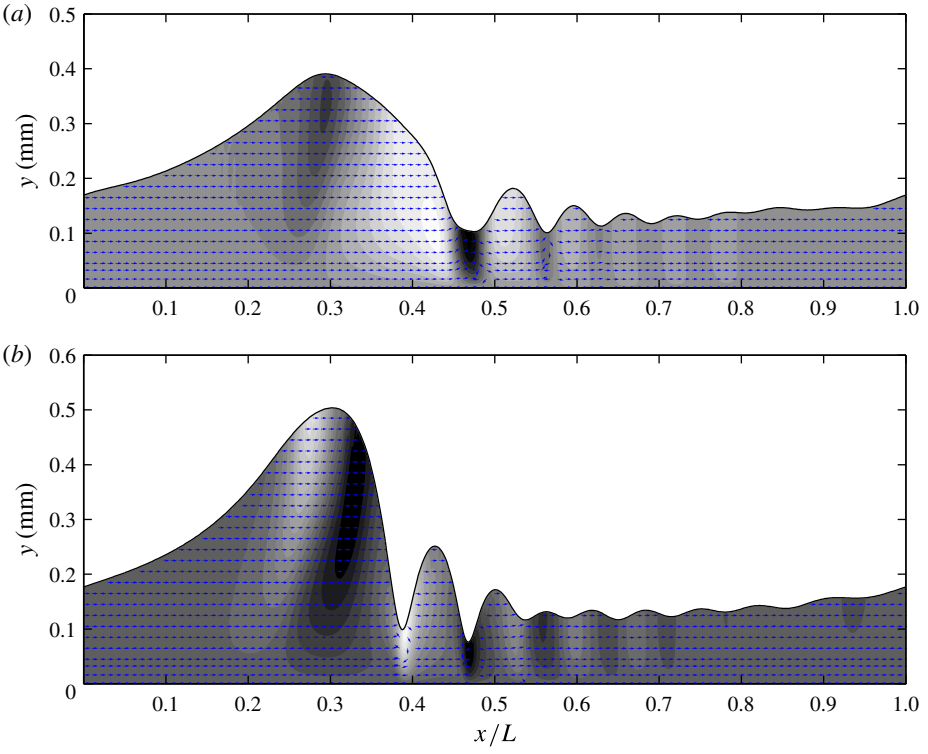


FIGURE 18. (Colour online) Case 2: velocity field projection into x–y slices at different spanwise positions in figure 17 (see also figure 14*b*): (*a*) $z/W = 0.4$ (black $w = -0.14$ m s^{-1}, white $w = 0.11$ m s^{-1}), $u_{min} = -0.02$ m s^{-1}; and (*b*) $z/W = 0.7$ (black $w = -0.04$ m s^{-1}, white $w = 0.10$ m s^{-1}), $u_{min} = -0.13$ m s^{-1} Arrows are normalized with their magnitude. Contours indicate spanwise velocity component.

local Reynolds numbers $\hat{Re}$ significantly in excess of the mean value Re. In this context, we also point out that it is in the large humps that Adomeit & Renz (2000) observed the initiation of interfacial turbulent spots.

5.2.2. *The visco-capillary region*

For cases 1 to 3, associated with large-Ka liquids, flow in the visco-capillary region is dominated by surface-tension-related pressure variations imposed by changes in total free- surface curvature κ. The wall pressure gradient there is in good approximation dictated by the interfacial pressure jump (neglecting viscous stresses):

$$\nabla p_w \approx \sigma \nabla \kappa, \quad \kappa = \kappa_{xy} + \kappa_{zy}. \tag{5.3}$$

This was established for two-dimensional films by Malamataris, Vlachogiannis & Bontozoglou (2002), who showed the relation to hold quantitatively in most regions of the film with the exception of capillary wave troughs, where larger normal velocities can occur (Dietze *et al.* 2008). However, (5.3) still holds qualitatively there. This can be seen in figure 19, evincing a close correlation between film thickness and wall pressure variations in the visco-capillary region. Importantly, in the three-dimensional

https://doi.org/10.1017/jfm.2013.679 Published online by Cambridge University Press

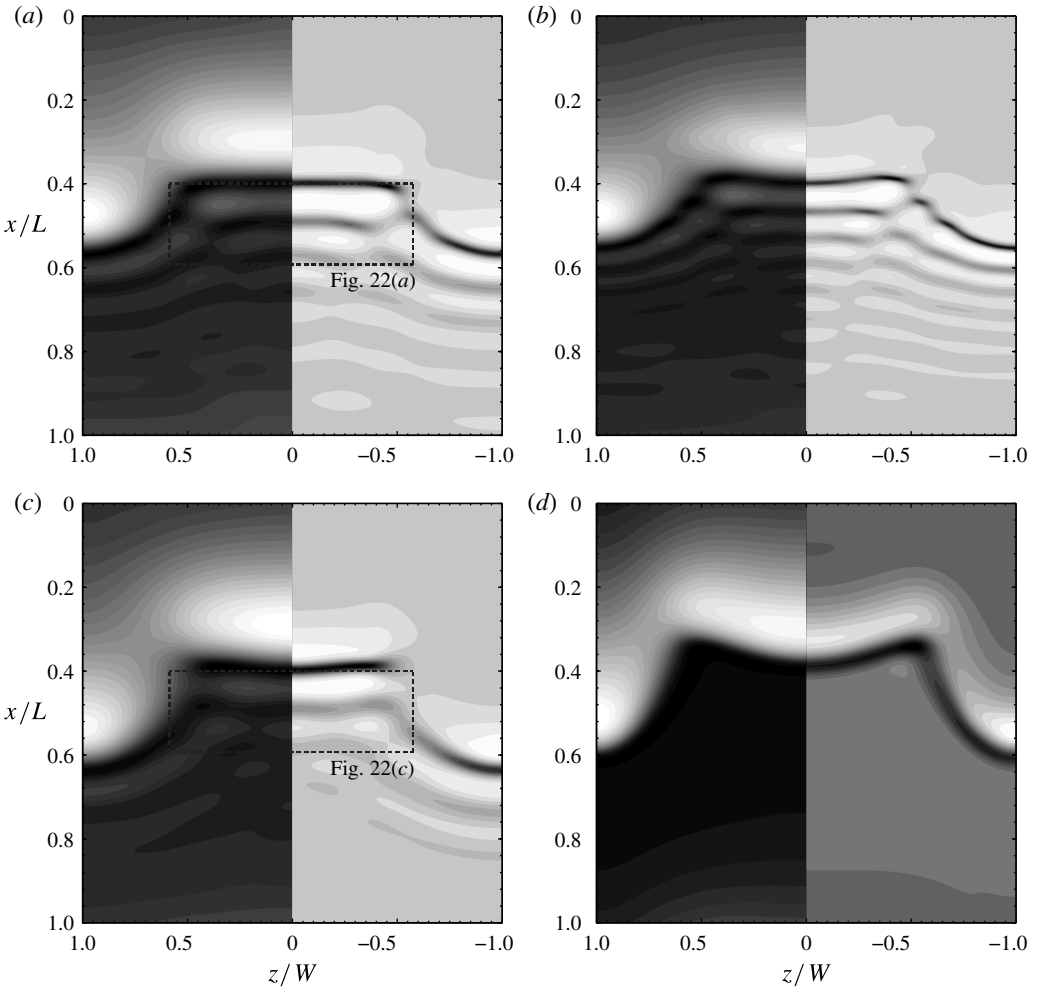


FIGURE 19. Contours of film thickness (left) and wall pressure (right). Levels from black to white are uniformly distributed between extremal values: (*a*) case 1, $t = 0.20$ s, (0.06, 0.45) mm and (−114, 27) N m^{-2}; (*b*) case 2, $t = 0.14$ s, (0.06, 0.60) mm and (−165, 41) N m^{-2}; (*c*) case 3, $t = 0.30$ s, (0.12, 0.64) mm and (−60, 17) N m^{-2}; and (*d*) case 4, $t = 0.28$ s, (0.49, 1.70) mm and (−8.3, 9.4) N m^{-2}. Boxes highlight area of view represented in figure 22.

flows considered here, κ is composed of contributions in the streamwise and spanwise directions:

$$\kappa_{xy} = \partial_{xx}\delta \left[1 + (\partial_x \delta)^2\right]^{-3/2}, \quad \kappa_{zy} = \partial_{zz}\delta \left[1 + (\partial_z \delta)^2\right]^{-3/2}. \tag{5.4}$$

Relations (5.3) and (5.4) enable one to explain two characteristic features of the visco-capillary region evinced by the previously introduced figures 13 and 14, showing maps of the local inverse Weber number and the wall shear stress components. We will at places refer back to these figures in what follows.

https://doi.org/10.1017/jfm.2013.679 Published online by Cambridge University Press

Firstly, streamwise changes in κ_{xy} can be sufficiently strong to impose an adverse pressure gradient surpassing the effect of gravity. This leads to flow separation (and associated backflow) at the wall in the troughs of the most pronounced capillary waves, as has been found in two-dimensional films (Malamataris *et al.* 2002; Dietze *et al.* 2008, 2009; Malamataris & Balakotaiah 2008). In the three-dimensional case, these separation zones are modulated by the spanwise shape of the capillary wave fronts, as shown in the streamwise wall shear stress plots of figure 14 (see left half-plane in panels *a* to *c*), where regions of flow reversal are delimited by black contour lines marking $\tau_{wx} = -\mu_l \partial_y u|_{y=0} = 0$. The number of these regions increases with the Kapitza and Reynolds numbers, the first quantifying the relevance of capillary forces and the second scaling the amplitude of large waves (and thus that of the resulting capillary waves). Panels (*a*) and (*b*) demonstrate the Reynolds number effect, while panel (*d*), showing results for the lowest Kapitza number case (i.e. case 4 with $Ka = 17$), exhibits no upflow zone.

For cases 1 to 3, flow reversal zones develop at the first few capillary troughs downstream of the leading and trailing humps. They are disconnected in spanwise direction at the interfacial saddle points, which are visible in the left half-planes of figure 13. Figure 20 depicts streamlines within the two symmetry planes ($z/W = 0$ and $z/W = 1$) for cases 1 and 2, showing the flow structure within these flow reversal zones. For both cases, large separation eddies occur at the first two capillary troughs preceding the trailing wave hump. The most upstream of these exhibits an open shape, while the second has a closed form. This is due to the smaller streamwise change in free-surface curvature at the second capillary trough and the associated smaller adverse pressure gradient there, as shown in figure 20(*c*). Downstream of the leading hump (see figure 20*b*) , the first capillary wave exhibits a separation zone with larger upstream velocity compared to the trailing hump (the adverse pressure gradient is twice as large, which is not shown here), while the second produces only a very small separation zone. Flow separation zones for case 2 (see figure 20*d*,*e*) are larger and associated with larger upstream velocities compared to case 1. This results from the larger-amplitude capillary waves developing in this case as a direct consequence of the larger main wave humps (compare also pressure distributions in figure 20*c*).

Meanwhile, spanwise flow in the visco-capillary region for cases 1 to 3 is entirely dominated by curvature-induced pressure variations due to the absence of gravity in this direction (the latter point has recently been made by Georgantaki *et al.* (2011)). This is illustrated representatively for case 1 (at a given streamwise z–y slice in the visco-capillary region) in figure 21, showing the occurrence of a cellular flow pattern within the spanwise succession of capillary humps and troughs. Here, the flow direction is imposed by the spanwise derivative of wall pressure as shown in figure 21(*b*). For case 4, where *Ka* is very low, the visco-capillary region displays almost no spanwise flow (see spanwise wall shear stress plot in figure 14*d*).

A second characteristic feature of the visco-capillary region is the three-dimensional nature of capillary waves downstream of the trailing wave hump for cases 1 to 3. Given the dominance of capillary forces there, a Plateau–Rayleigh type mechanism conceivably plays a role. As in our three-dimensional case, the contributions of κ_{xy} and κ_{zy} (equations (5.4)) can be counteracting, the total free-surface curvature κ may increase from local minima to local maxima, driving flow away from capillary troughs. Figure 22, displaying a blown-up view of the visco-capillary region, shows that this indeed occurs. Here, we have plotted contours of the wall pressure gradient (left half-plane) and wall shear stress (right half-plane) projected in the direction of the film thickness gradient, i.e. $\nabla p_w \cdot \nabla\delta$ and $\boldsymbol{\tau}_w \cdot \nabla\delta$, respectively ($\boldsymbol{\tau}_w = [\tau_{wx}, \tau_{wz}]^{\mathrm{T}}$). Contour shades are adjusted such that only regions with negative values for these quantities are

https://doi.org/10.1017/jfm.2013.679 Published online by Cambridge University Press

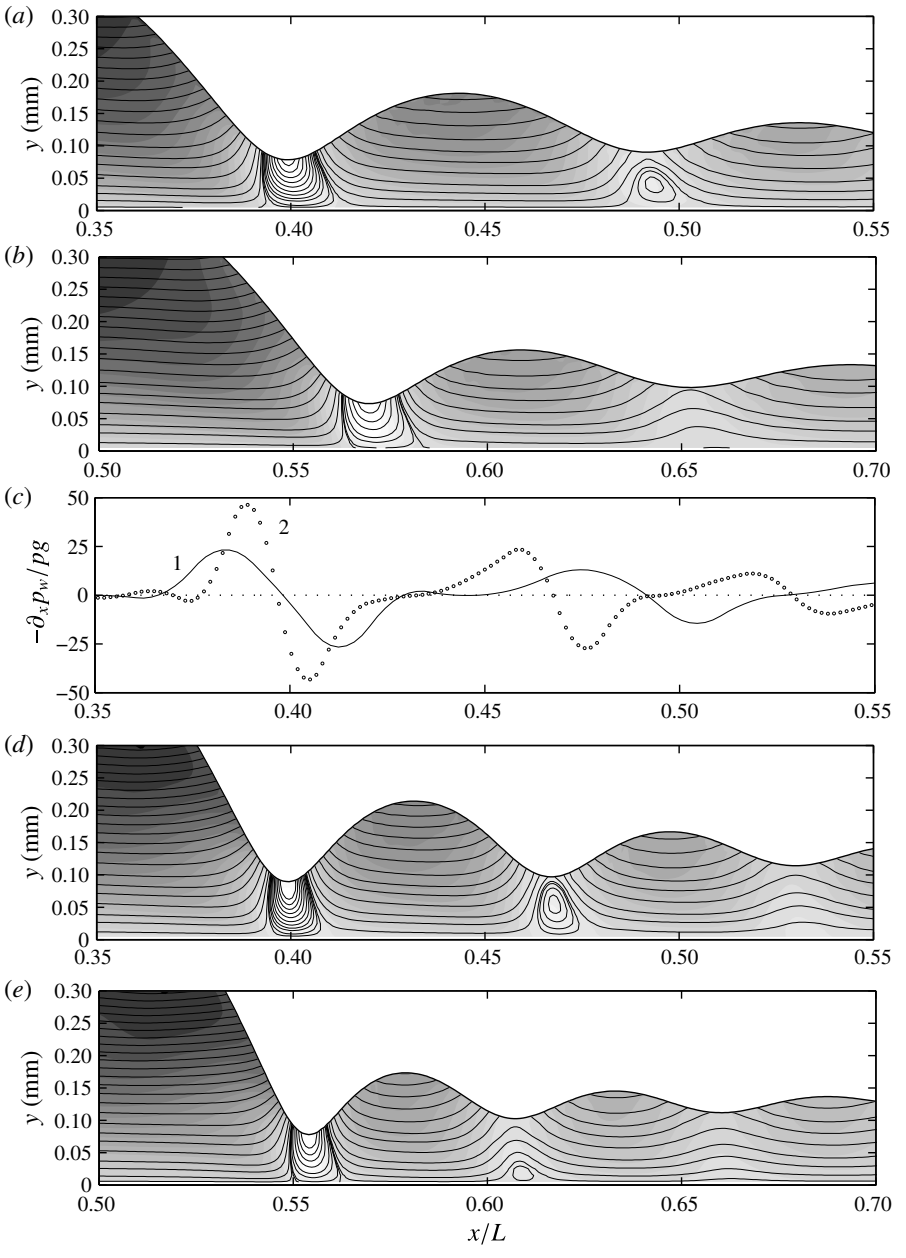


FIGURE 20. Cases 1 and 2: streamlines and streamwise wall pressure gradient in spanwise symmetry planes (see figure 14). (*a*) Case 1 ($t = 0.2$ s): $z/W = 0$ (black $u = 0.37$ m s^{-1}, white $u = -0.14$ m s^{-1}). (*b*) Case 1 ($t = 0.2$ s): $z/W = 1$ (black $u = 0.40$ m s^{-1}, white $u = -0.15$ m s^{-1}). (*c*) Streamwise wall pressure gradient for panels (*a*) (solid line) and (*d*) (circles). (*d*) Case 2 ($t = 0.14$ s): $z/W = 0$ (black $u = 0.46$ m s^{-1}, white $u = -0.15$ m s^{-1}). (*e*) Case 2 ($t = 0.14$ s): $z/W = 1$ (black $u = 0.53$ m s^{-1}, white $u = -0.20$ m s^{-1}). Contours (equidistantly valued) indicate streamwise velocity.

https://doi.org/10.1017/jfm.2013.679 Published online by Cambridge University Press

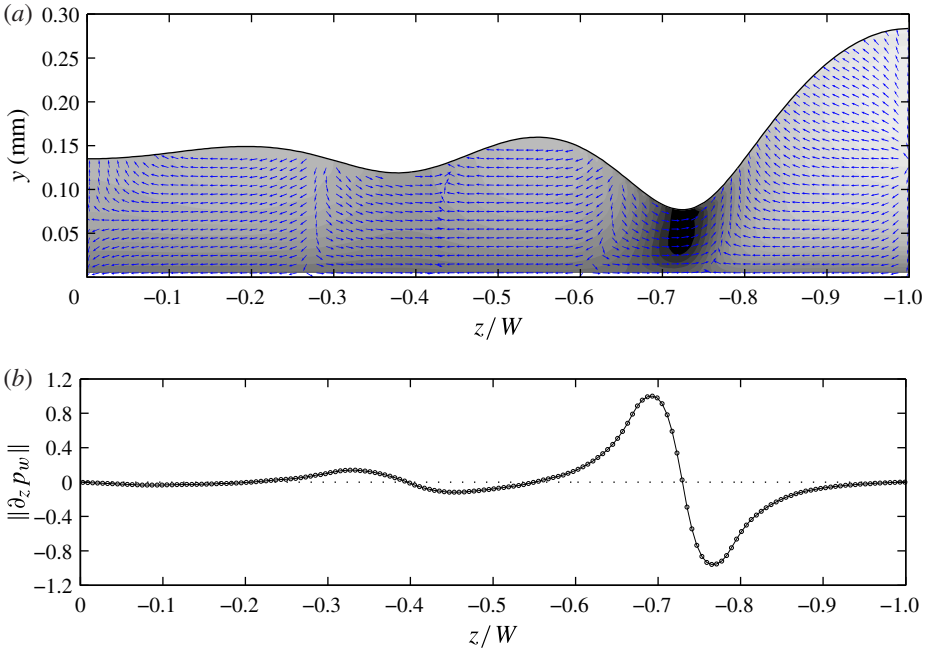


FIGURE 21. (Colour online) Case 1 ($t = 0.2$ s): spanwise flow in the visco-capillary region. (*a*) Velocity field projection into z–y slice at representative streamwise position ($x/L = 0.54$ mm, see figure 13*a*): $u_{min} = -0.09$ mm s^{-1}, $u_{max} = 0.38$ mm s^{-1}, $|w|_{max} = 0.08$ mm s^{-1}. Arrows are normalized with their magnitude and contours indicate streamwise velocity component. (*b*) Spanwise wall pressure derivative (normalized with largest absolute value).

visible. Within these so-designated *destabilizing regions*, wall pressure decreases from wave trough to wave hump and the flow (near the wall) is directed away from the troughs. These regions do not occur exactly at the local extrema, as both curvature contributions have the same sign there. They are rather associated with the slopes between extrema, where κ_{xy} and κ_{zy} are opposed.

In the *streamwise* direction, gravity overshadows the effect of the destabilizing pressure variations, as can be seen in more detail in figure 23, showing the velocity field within a near-wall x–z slice for case 2 (only the right half-plane is shown here). Where the destabilizing regions lie upstream of a local maximum, gravity already causes a flow from minimum to maximum, while in the converse case, the pressure gradient (in most regions) is not sufficiently large to counteract gravity and force liquid towards an upstream hump. However, the three most upstream capillary minima (see positions 1, 2 and 3 in figure 23) do indeed force flow away in all directions. In the *spanwise* direction, liquid is channelled towards interfacial saddle points (abbreviated with 'SP') in the vicinity of local extrema highlighted with plus and minus signs in figure 23. This can be seen most clearly below the local minimum at position 1, where liquid is drained in the spanwise direction towards the SP on the left. *Channelling* results from the distribution of total free-surface curvature, the contour levels of which are also shown in figure 23. Local maxima (where curvature is negative and liquid pressure thus high) act as repellants, 'squeezing' the flow into the troughs of the capillary waves, which are modulated by an alternation

https://doi.org/10.1017/jfm.2013.679 Published online by Cambridge University Press

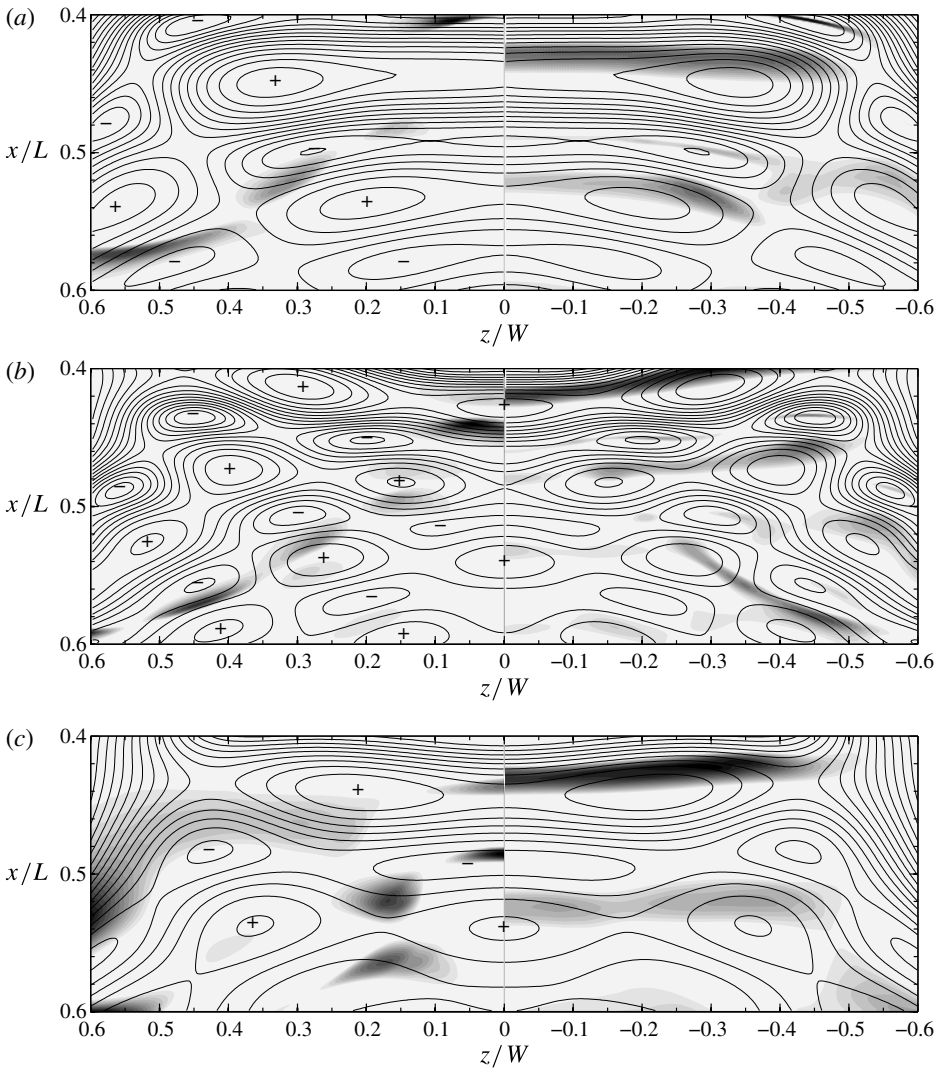


FIGURE 22. Zoom on the visco-capillary region in figure 19. Contours of wall pressure gradient ∇p_w (left, $\nabla p_w \cdot \nabla\delta$) and wall shear stress $\boldsymbol{\tau}_w = [\tau_{wx}, \tau_{wz}]^{\mathrm{T}}$ (right, $\boldsymbol{\tau}_w \cdot \nabla\delta$) projected in the direction of the film thickness gradient $\nabla\delta$ with $\nabla = [\partial_x, \partial_z]^{\mathrm{T}}$: (*a*) case 1, $t = 0.2$ s (see figure 6*e*); (*b*) case 2, $t = 0.175$ s (see figure 7*e*); and (*c*) case 3, $t = 0.3$ s (see figure 8*f*). Contour levels show only negative values, highlighting regions of three-dimensional instability where flow and pressure gradient are (partially) in the direction of increasing film thickness. For case 2, a more unstable time point than in figure 19 is shown. Solid lines represent film thickness isolevels and signs mark local maxima (+) and minima (−).

of local minima and saddle points. Within these troughs, the flow is once again directed towards the SPs, which is a specific feature of three-dimensional falling films, resulting from the competition of different curvature contributions.

An interesting conclusion then is that the spanwise separation of large waves is coupled with the streamwise curvature of the precursory capillary waves through

https://doi.org/10.1017/jfm.2013.679 Published online by Cambridge University Press

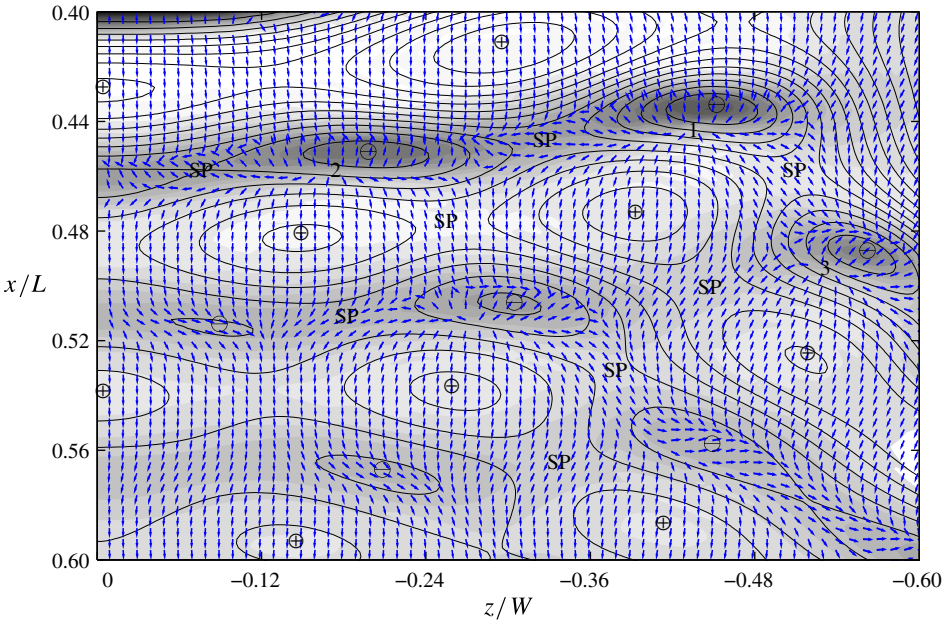


FIGURE 23. (Colour online) Case 2 ($t = 0.175$ s): flow in the region of capillary wave interaction. Velocity field projection into near-wall x–z slice ($y = 0.04$ mm). Arrows are normalized with their magnitude, contour levels indicate total free-surface curvature $\kappa = \kappa_{xy} + \kappa_{zy}$ ($\kappa_{xy}^{max} = 4$ mm^{-1}) and contour lines show film thickness δ (plus and minus signs indicate local maxima and minima and SP designates saddle points): white, $\kappa_{min} = -0.52$ mm^{-1}; black, $\kappa_{max} = 2.0$ mm^{-1}.

a Plateau–Rayleigh type instability. However, the instability mechanism is more complicated than for a liquid cylinder, as volume is not conserved within a capillary wave. Nonetheless, the maximal streamwise curvature of such a wave in figure 23 is $\kappa_{xy}^{max} = 4$ mm^{-1}, yielding a 'most dangerous' wavelength of $\Lambda_{PR}^{max} = 2\pi R/0.697 = 2.3$ mm for the Plateau–Rayleigh instability of a liquid cylinder of radius $R = 1/\kappa_{xy}^{max}$. This is not far from the spanwise separation of local maxima along a capillary wave in figure 23 (≈3 mm).

5.3. *Oscillation between two- and three-dimensional waves: governing mechanism*

In figure 12, it was observed that surface waves for the four considered cases oscillate between two- and three-dimensional topologies. We have found that these oscillations result from an interaction between the two distinct flow regions discussed in §§ 5.2.1 and 5.2.2, i.e. between the inertia-dominated region and the visco-capillary region. A similar observation was made for *two-dimensional* falling liquid films by Pradas, Tseluiko & Kalliadasis (2011) and Pradas, Kalliadasis & Tseluiko (2012), who found oscillating interactions between subsequent wave humps preceded by a large number of capillary waves. When two such humps approach one another, the capillary waves are compressed and streamwise curvature changes are increased. In this context, Pradas *et al.* (2013) have recently demonstrated the existence of overdamped, underdamped and self-sustained oscillations around bound states in two-dimensional films. For our *three-dimensional* situation, we find that the capillary waves play a similar yet subtly different role for the dynamics of large humps.

https://doi.org/10.1017/jfm.2013.679 Published online by Cambridge University Press

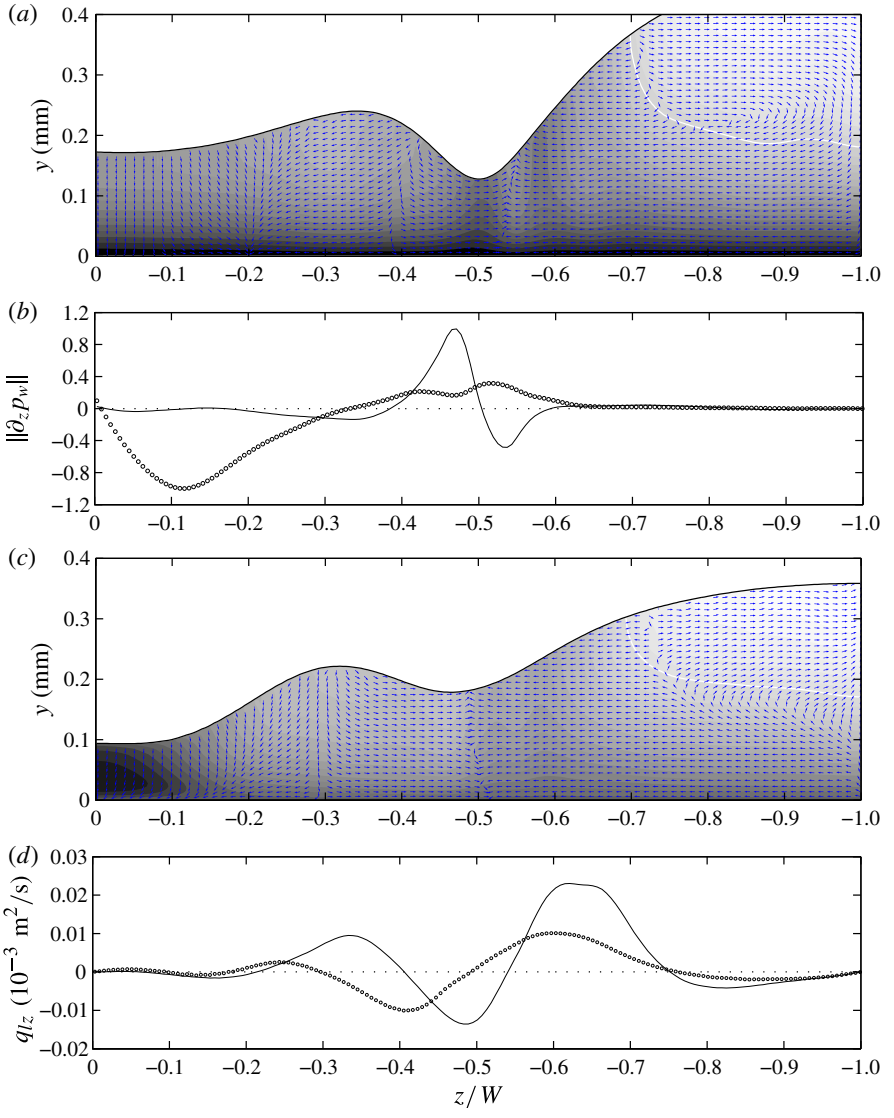


FIGURE 24. (Colour online) Case 2: capillary draining of the leading hump. (*a*,*c*) Velocity field projection into *z*–*y* slices at the streamwise position of first capillary wave crest for different time points (see figure 7): (*a*) $t = 0.14$ s, $x/L = 0.42$ ($u_{min} = 0.002$ m s^{-1}, $u_{max} = 0.61$ m s^{-1}), $|w|_{max} = 0.13$ m s^{-1}; (*c*) $t = 0.175$ s, $x/L = 0.40$ ($u_{min} = -0.1$ m s^{-1}, $u_{max} = 0.5$ m s^{-1}), $|w|_{max} = 0.08$ m s^{-1}. (*b*) Spanwise wall pressure derivative (normalized with largest absolute value) and (*d*) spanwise flow rate q_{lz} (compare with $\bar{\bar{q}}_{lx} \approx Re^{tgt} \nu_l = 0.05 \times 10^{-3}$ m^2 s^{-1}). Solid lines and symbols corresponds to $t = 0.14$ s and $t = 0.175$ s, respectively. Arrows are normalized with their magnitude and contours indicate streamwise velocity component (white contour line corresponds to wave celerity $c = f\Lambda_x$).

More specifically, we have found the oscillation between two- and three-dimensional interfacial structures to be associated with the first precursory capillary wave. We explain the governing mechanism here based on data for case 2. For this, we will occasionally refer back to the previously introduced figures 7, 10 and 13(*b*). A more vivid view is provided in the supplementary movie Case2_DNS for case 2 (DNS).

https://doi.org/10.1017/jfm.2013.679 Published online by Cambridge University Press

To start, we recall figure 7, where it was observed in a first stage, between $t = 0.075$ s and $t = 0.14$ s, that the trough of the first precursory capillary wave is gradually deformed by the streamwise protrusion of the large leading humps. This produces an increasing spanwise component of free-surface curvature there, which is more clearly visible in figure 24(*a*), showing a z–y slice at the streamwise position of the first capillary wave hump's central portion for $t = 0.14$ s (figure 13*b* highlights this position). Owing to capillary forces, this spanwise curvature produces a spanwise pressure gradient (plotted in figure 24*b*) directed from the large hump to the capillary trough, which 'drains' liquid from the hump. The associated spanwise flow rate per unit width q_{lz}, which is plotted in figure 24(*d*), is very large and comparable to the mean streamwise flow rate $\bar{\bar{q}}_{lx}$ (this results from the absence of gravity as a counteracting force in the spanwise direction). As a consequence, the amplitude of the large hump is decreased and its width increased, which is clearly visible when comparing figure 24(*a*) and (*c*). These modifications of the leading hump's shape cause it to decelerate with respect to the trailing hump until the streamwise separation between the two saturates ($t = 0.175$ s in figure 10*a*). During this second stage ($t = 0.14$ s to $t = 0.175$ s in figure 7), the capillary trough swells (to such an extent that the first capillary wave bridges the left and right leading humps), reducing the driving pressure difference between leading hump and capillary trough as well as the associated spanwise flow rate plotted in figure 24(*d*). Incidentally, a similar sequence of events occurs at the second capillary wave, which is however less pronounced. Finally, in the third stage of the oscillatory dynamics ($t > 0.175$ s in figure 7), the streamwise separation of large humps decreases, whereby the free surface reverts more and more to a two-dimensional shape.

The above explanation in principle also applies to all other cases (1, 3 and 4), which were also shown to display oscillating dynamics in figure 12. For case 4, a more detailed discussion is necessary. For this case, there are no bridging capillary waves between the large leading humps. However, spanwise interfacial curvature and a resulting spanwise pressure gradient at the lone capillary trough are nonetheless produced when the leading humps protrude in streamwise direction (see figure 15*c*,*d*) and, consequently, the above-mentioned 'draining' mechanism still takes place. This explains the oscillatory dynamics in the first stage of figure 12(*d*) (up to roughly 15 periods), where the streamwise distance between leading and trailing humps fluctuates. Although the amplitude of deformation energy oscillations is small in the context of figure 12(*d*), it is rather large in comparison with the other cases in figure 12. At first sight, this observation is counter-intuitive, as the low Kapitza number for case 4 ($Ka = 17.8$) indicates that the capillary draining mechanism governing the first stage of the oscillatory dynamics is weak. However, it is precisely this weakness that allows the leading humps to protrude further downstream than in the other cases before they slow down and re-approach the trailing hump. Moreover, lowering Ka increases the amplitude of these humps (compare different cases in figure 13), making them less responsive to the draining mechanism. As a consequence of the above effects, the surface deformation energies E_x and E_z in figure 12(*d*) undergo larger changes. Further, it is observed in the WRIBL supplementary movie Case4_DNS for case 4, that the maximal separation between leading and trailing humps increases at each oscillation, until the spanwise coherence of the wave front is finally breached, entering the second stage of the oscillatory dynamics (after roughly 15 periods in figure 12*d*). As was pointed out when discussing figure 12 in § 5.1, oscillations in the deformation energies E_x and E_z then result from the leading humps repeatedly overtaking the trailing humps, which causes even larger oscillation amplitudes.

https://doi.org/10.1017/jfm.2013.679 Published online by Cambridge University Press

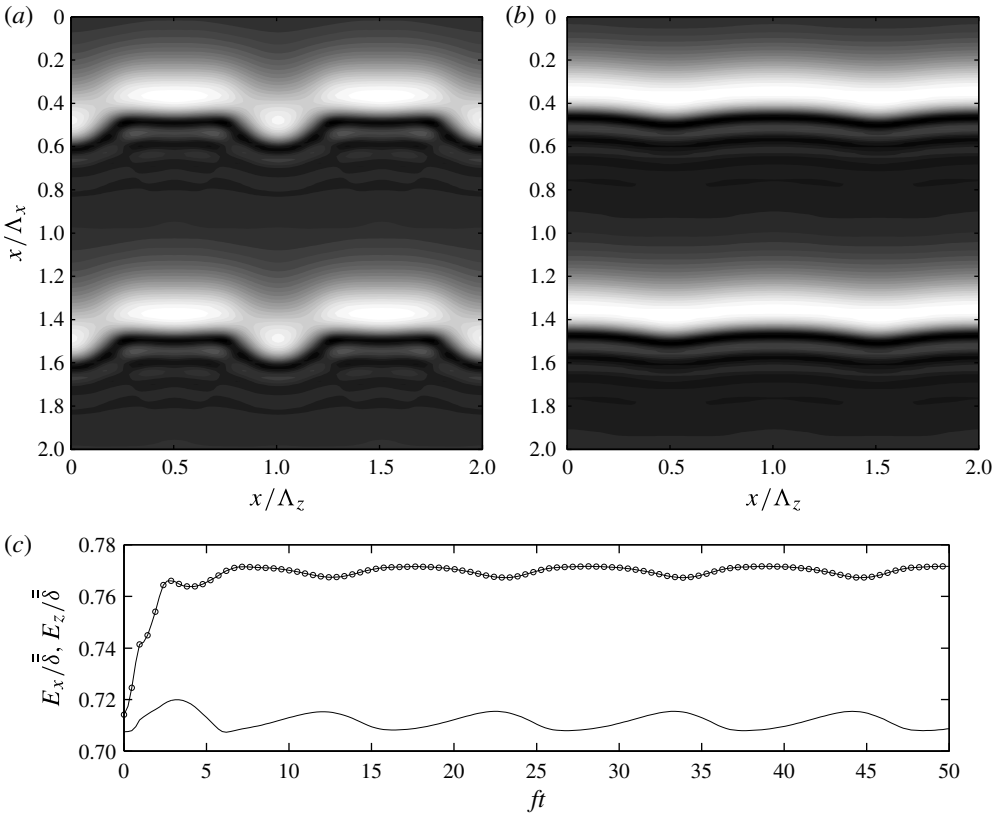


FIGURE 25. Long-time WRIBL simulation of case 3 on a domain of two wavelengths in the streamwise and spanwise directions, evincing oscillating wave dynamics. (*a*,*b*) Film thickness contours (black, minimum; white, maximum) at selected time points, (*a*) $ft = 4.6$ and (*b*) $ft = 15.5$, showing pronounced three-dimensional and more two-dimensional wave structures. (*c*) Time traces of surface deformation energies E_x and E_z evaluated based on equations (5.1*a*) and (5.1*b*): symbols, $E_x/\bar{\bar{\delta}}$; solid line, $E_z/\bar{\bar{\delta}}$.

Finally, it may be asked whether the observed oscillations for cases 1 to 4 possibly result from the constraint imposed by using computational domains of a single streamwise wavelength. We check this based on a WRIBL simulation of case 3 performed on a domain of two wavelengths in the spanwise and streamwise directions (simulations of case 3 on a 4×4 domain and case 4 on a 2×2 domain, not shown here, lead to equivalent results). For this case, agreement between single-wave WRIBL simulation and corresponding DNS is best. Figure 25(*c*) shows time traces of the deformation energies E_x and E_z (equations (5.1*a*) and (5.1*b*)) for the 2×2 simulation. It shows oscillating wave dynamics to persist, in good agreement with the single-wave results in figure 12(*c*) (only a slight shift in oscillation frequency occurs). In addition, figure 25(*a*,*b*) shows film thickness contours of distinctly three- and more two-dimensional wave structures at two characteristic time points within the oscillation. We have provided a supplementary movie Case3_WRIBL_2x2 (and a similar one, movie Case4_WRIBL_2x2, for case 4), showing oscillations between these two types of structures.

https://doi.org/10.1017/jfm.2013.679 Published online by Cambridge University Press

The oscillatory wave dynamics observed in figure 12 are thus not an artefact of the employed computational domain, and result from an interaction between the visco-capillary region, which produces flows governed by free-surface curvature, and the inertia-dominated region, which is governed by the gravity-driven Kapitza instability. This interaction is distinctly three-dimensional and governed by the spanwise curvature of the first precursory capillary trough. We also point out that the earlier-mentioned experiments by Alekseenko *et al.* (2012), conducted on vertically falling liquid films similar to case 2, have evinced oscillations of the streamwise distance between leading and trailing humps as well as overtaking events during the downward propagation of wave packets.

5.4. *Influence of surface waves on the gas phase*

To conclude our analysis of the velocity field, we focus on the gas phase in this last subsection by studying case 1 representatively. Figure 26 shows the time evolution of streamlines within the symmetry plane $z/W = 1$ (see figure 1) for this case, as a surface wave of growing amplitude passes through the gas. In the first stage, when the wave is of small amplitude and close to sinusoidal, a large vortex seems to occur above the wave hump. The computational domain is open at the top, so that this vortex is pushed out and is only partially visible. In the case of a wall-bounded domain, Dietze & Ruyer-Quil (2013) have shown a similar vortex in the case of an aerostatic pressure drop in the gas. We point out that, due to the periodic boundary conditions employed here (which apply also to pressure), gas flow conditions in the current study are quite different and less realistic. In a second stage (last three panels), during which the wave shape becomes more complicated, capillary waves preceding the large hump generate the separation zones discussed with respect to figure 20. These are seen here to transcend the free surface into the gas, where they assume a closed shape. This induces crosswise mixing lengths of relatively large amplitude in the gas immediately downstream of the large wave hump, which are noticeable up to a relatively large wall distance.

Based on the argument that there is no gravity component in the spanwise direction, it is expected that even larger flow structures of this kind occur within horizontal z–y slices of the flow. This is illustrated by figure 27, showing a spanwise succession of four very large counter-rotating vortices in the gas at a streamwise position slightly downstream of the leading wave crest ($x/L = 0.54$). Each vortex is associated with one of the capillary wave humps or troughs and extends down into the liquid film. The height of these vortices ($y/H > 0.5$) significantly surpasses the amplitude of the leading hump, which corresponds to $y \approx 0.45$ mm, i.e. $y/H \approx 0.375$ (see figure 15*a*).

6. Conclusion

We have numerically investigated the nonlinear wave and flow dynamics of vertically falling liquid films with three-dimensional regular surface waves consisting of large-amplitude horseshoe-shaped humps preceded by capillary ripples. Our analysis is based on full numerical simulations of periodic wave segments (performed on the Juropa supercomputer at Forschungszentrum Jülich) as well as long-time simulations using the low-dimensional model of Scheid *et al.* (2006). Four flow situations related to previously published experiments (Nosoko *et al.* 1996; Dietze *et al.* 2009; Rohlfs *et al.* 2012), using working liquids covering a large range of Kapitza number values $Ka = \sigma\rho_l^{-1}\nu_l^{-4/3}g^{-1/3} = 18$–$3923$, were considered. The first two cases concern water films of increasing Reynolds number, approaching the threshold ($Re = 75$) at

https://doi.org/10.1017/jfm.2013.679 Published online by Cambridge University Press

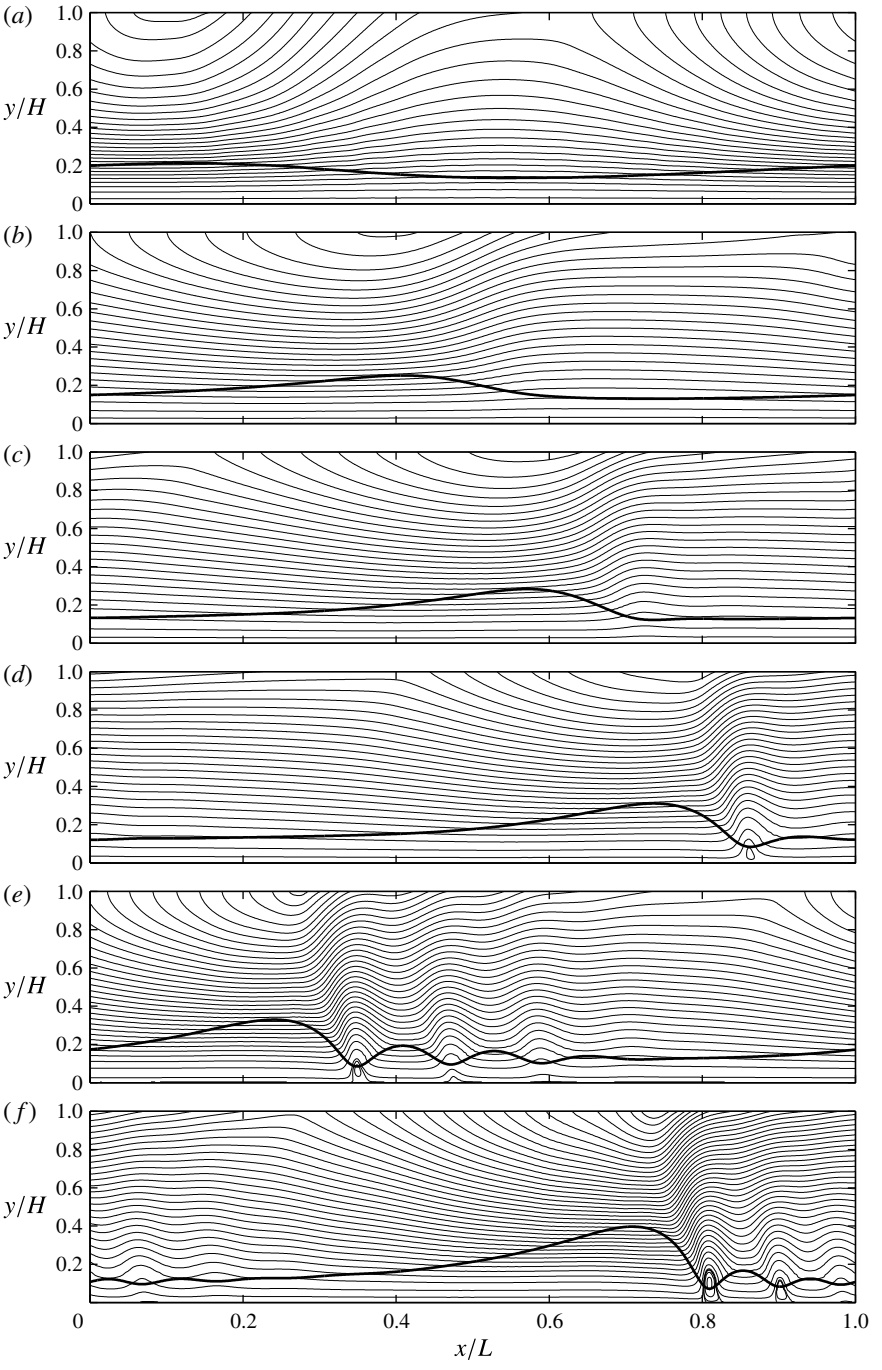


FIGURE 26. Case 1 (DNS): reaction of the gas phase to a surface wave of growing amplitude passing through it. Streamlines are drawn within the symmetry plane $z/W = 1$ and time points (from top to bottom) are $t = 0.005$ s, 0.02 s, 0.03 s, 0.04 s, 0.07 s and 0.2 s, respectively. Panels represent the entire computational domain and stream function values vary between panels.

https://doi.org/10.1017/jfm.2013.679 Published online by Cambridge University Press

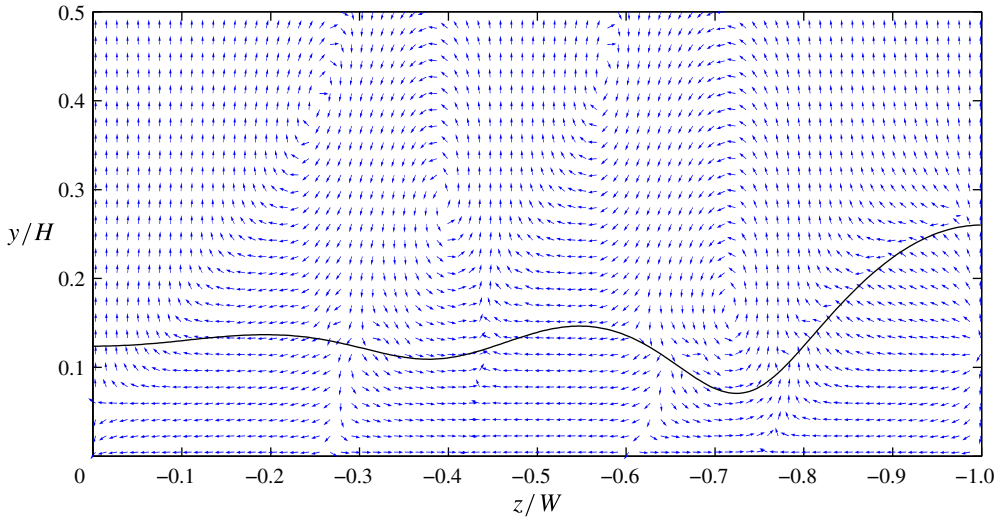


FIGURE 27. (Colour online) Case 1: $t = 0.2$ s, $x/L = 0.54$. Velocity field projection into a z–y slice slightly downstream of the leading wave crest showing both fluid phases (vectors are normalized with their magnitude). Spanwise film thickness and curvature modulations associated with capillary waves generate a cellular pattern of four large counter-rotating vortices in the gas.

which wave-induced intermittent turbulence has been experimentally observed (Ishigai *et al.* 1972). Here, the Kapitza number is very large ($Ka = 3923$) and capillary forces dominate viscous forces, leading to a large number of precursory capillary ripples, while in cases 3 ($Ka = 509$, DMSO–water) and 4 ($Ka = 18$, silicone oil) Ka is reduced to very low values, at which viscous dissipation becomes dominant, eventually resulting in a thin precursory residual film without capillary ripples.

The evolution of the nonlinear three-dimensional waves from a small-amplitude initial perturbation is similar for all cases. In the early stages, a mainly two-dimensional large wave, which produces an increasing number of capillary ripples, develops as a result of a selective initial condition, prescribing a larger perturbation amplitude in the streamwise than in the spanwise direction. The spanwise perturbation then distorts the large wave front into a central part (designated as *trailing hump*) trailing the outer portions (designated as *leading humps*). The streamwise distance between leading and trailing humps increases over time, deforming the preceding capillary ripples, which develop spanwise interfacial curvature in the process. Eventually, saddle points occur on successive wave fronts at the intersection of the leading and trailing wave portions. The trailing portion assumes an almost horizontal 'table-top' shape, while the leading part remains curved in the shape of a horseshoe. Meanwhile, for the large-Ka liquids, the first capillary waves disconnect and form spanwise liquid bridges between the leading horseshoe humps.

We show that the observed wave topology segregates the liquid film into two regions of distinctly different flow dynamics. Within the large humps, the local Reynolds number $\hat{Re} = q_{lx}/\nu_l$ can be up to five times larger than its mean value, and the local Weber number $\hat{We} = \sigma\delta/(\rho q_{lx}^2)$ assumes globally low values. Consequently, inertia dominates the effect of viscous and capillary forces, resulting in a number of complex flow structures of different scale in this region. Two three-dimensional

https://doi.org/10.1017/jfm.2013.679 Published online by Cambridge University Press

moving frame vortices with crosswise (i.e. normal to the bounding wall) vorticity, spanning the entire height of the wave, occur in the leading hump. These intensify convective transport and by extension the transfer of a scalar transport variable. In the trailing hump (which exhibits only moderate film thickness variations in spanwise direction), a complex pattern of vorticity-carrying structures, which are only weakly related to spanwise film thickness variations, has been observed. These intermittent structures originate at the wall and result from the interaction between pressure gradients of capillary origin and the inertia of the main flow. They could play a role in the generation and/or selection of turbulent flow structures at higher Reynolds numbers. Moreover, the wave-induced segregation of the flow into an inertia-dominated and a visco-capillary region, and the associated peaks in $\hat{Re}$, explain why turbulence in films is observed at much lower mean Reynolds number values than in single-phase plane Poiseuille flows and why it is initially intermittent. Here, the term 'turbulence' refers to three-dimensional bulk turbulence and needs to be distinguished from the weak turbulence (Manneville 2004) to which the free-surface topology of falling liquid films is prone. The latter may occur in the form of two-dimensional (Chang, Demekhin & Kalaidin 1996*a*) or three-dimensional (Demekhin *et al.* 2007*a*) interfacial chaos composed of wave packets generated by the interplay between the inertia of the large humps and dissipation within the small capillary waves.

In the region separating the large humps, $\hat{Re}$ and $1/\hat{We}$ are low and viscous/capillary forces dominate inertia. For the large-Ka liquids (at low Ka, a very thin almost entirely flat residual film occurs), flow in this region is dominated by pressure gradients imposed by variations in total free-surface curvature through the action of capillary forces. This leads to streamwise separation zones underneath the capillary troughs, and a cellular spanwise flow pattern in the region of capillary wave interference.

Overall, the flow dynamics in three-dimensional films differ significantly from those in two-dimensional films due to the absence of gravity in the third (spanwise) direction. This leads to the complex inertia- and capillary-dominated flow structures described above. Moreover, we have confirmed the existence of destabilizing zones in the visco-capillary region of high-Ka films. These are characterized by pressure gradients driving the flow from local capillary minima to maxima due to a corresponding increase in (total) free-surface curvature and are thus related to the Plateau–Rayleigh mechanism. Finally, our long-time simulations, performed with the WRIBL model of Scheid *et al.* (2006), evince oscillations between three- and two-dimensional wave patterns (first reported by Alekseenko *et al.* (2012) and Kalliadasis *et al.* (2012)) caused by spanwise coupling between capillary ripples and large humps. Such coupling has been observed in the streamwise direction for two-dimensional liquid films (Malamataris *et al.* 2002; Pradas *et al.* 2011, 2012). In our three-dimensional case, capillary waves bridging the large horseshoe humps drain liquid from the latter by capillary suction, decreasing their amplitude and wave celerity in regard to the trailing hump. This reduces the separation between the two and causes the flow to revert back to a more two-dimensional pattern, preventing the three-dimensional waves from assuming a developed state.

Finally, we have considered the effect of the studied three-dimensional surface waves and associated flow structures on the flow field in the surrounding gas. Two-dimensional investigations have shown that intricate vorticity-carrying structures in the gas can occur due to the waviness of the free surface (Nave 2004; Dietze & Ruyer-Quil 2013). Our simulations show that such structures are even more intricate in the three-dimensional case, as there is no gravity component in the spanwise

https://doi.org/10.1017/jfm.2013.679 Published online by Cambridge University Press

direction. This causes a series of very large counter-rotating vortices seen within a plane normal to the main direction of the flow in the capillary wave region downstream of the trailing hump. These vortices are associated with successive spanwise capillary humps and troughs and extend far beyond the height of the large wave humps. Such structures potentially intensify inter-phase heat and mass transfer and may even play a role in the destabilization of two-dimensional surface waves towards three-dimensional structures, suggesting two interesting routes for future research.

Acknowledgements

Funding for G.F.D. was partially provided by DAAD (Deutscher Akademischer Austauschdienst) in the context of a postdoctoral scholarship. He also acknowledges programming contributions by Martin Horsky and fruitful discussions with Nicolas Kofman, Christian Ruyer-Quil and Sophie Mergui. Funding for W.R. was provided by DFG (Deutsche Forschungsgemeinschaft) under grant number KN-764-3-2. B.S. thanks the FRS-FNRS for funding. We also acknowledge the financial support of EU-FP7 ITN Multiflow. Direct numerical simulations were mainly performed on the Juropa supercomputer at Forschungszentrum Jülich under grant number HAC27. We also acknowledge generous access to the high-performance cluster of the Institute for Scientific Computing at RWTH-Aachen and the help of Martin Bücker.

Supplementary movies

Supplementary movies are available at http://dx.doi.org/10.1017/jfm.2013.679.

Appendix. WRIBL simulation results for comparison with DNS

Figures 28–31 show the time evolution of the three-dimensional free-surface topology for cases 1 to 4 as obtained from the WRIBL model of Scheid *et al.* (2006) (supplementary movies Case1_WRIBL–Case4_WRIBL are also provided), which is based on the approach introduced by Ruyer-Quil & Manneville (2000, 2002). These are to be compared with the DNS results in figures 6–9. Because the quantitative time evolutions of WRIBL simulations and DNS differ, we have displayed characteristic rather than exactly matching time points here. Comparison shows that the first phases of wave development (roughly the first three panels) are satisfactorily captured by the model, although horizontal portions of wave fronts are in general less wide for the WRIBL data. This is possibly due to the fact that DNS were performed over half a spanwise wavelength, using symmetry boundary conditions, while WRIBL simulations (due to the use of a spectral numerical method) were performed over a full spanwise wavelength, imposing periodic boundary conditions. The later stages of wave development are less well captured for cases 1 and 2, which display a very complex capillary interference pattern, while for cases 3 and 4, agreement remains good and fair, respectively. In the latter case, the applicability of the IBL approach is stretched due to the low Weber number of the flow ($We = 1.1$) (Gjevik 1970). For case 1, discrepancy with respect to the DNS data is due to an overshoot of the large leading humps, which protrude further downstream. However, the case later reverts back to a more two-dimensional wave topology in better agreement with the DNS (figure 28*f*). This retrogression to a more two-dimensional free surface (which is also visible in figure 30*f*) is the phenomenon studied by way of long-time WRIBL simulations in § 5.1 (see figure 12). As the most characteristic features of the wave

https://doi.org/10.1017/jfm.2013.679 Published online by Cambridge University Press

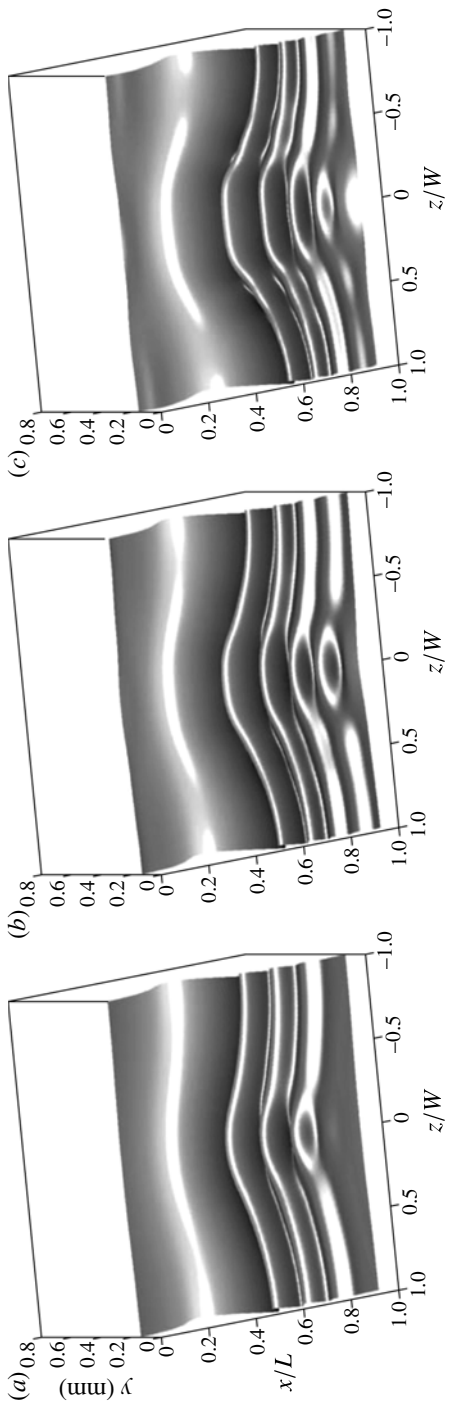


FIGURE 28. Case 1 (WRIBL): $Re^{tgt} = 40.8$, $f^{tgt} = 19.1$ Hz, $Ka = 3923$, $L = 20$ mm, $W = 10$ mm. Time evolution of free surface (compare to figure 6): (*a*) $t = 0.073$ s; (*b*) $t = 0.10$ s; (*c*) $t = 0.124$ s; (*d*) $t = 0.14$ s; (*e*) $t = 0.18$ s; (*f*) $t = 0.57$ s.

https://doi.org/10.1017/jfm.2013.679 Published online by Cambridge University Press

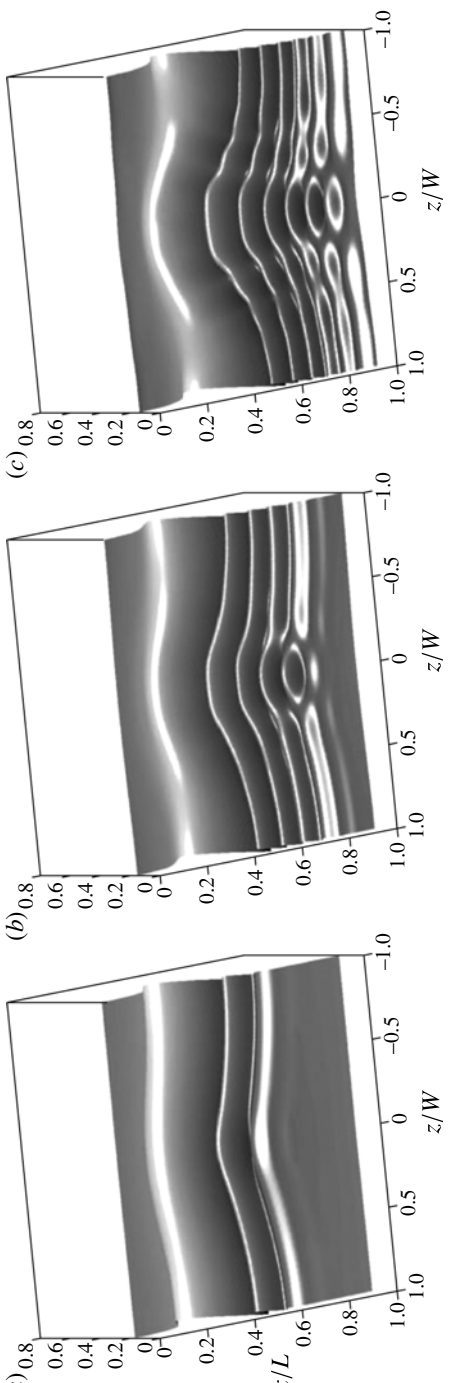


FIGURE 29. Case 2 (WRIBL): $Re^{ftgt} = 59.3$, $f^{ftgt} = 17$ Hz, $Ka = 3923$, $L = 25$ mm, $W = 10$ mm. Time evolution of free surface (compare to figure 7): (*a*) $t = 0.048$ s; (*b*) $t = 0.075$ s; (*c*) $t = 0.100$ s; (*d*) $t = 0.123$ s; (*e*) $t = 0.14$ s; (*f*) $t = 0.175$ s.

https://doi.org/10.1017/jfm.2013.679 Published online by Cambridge University Press

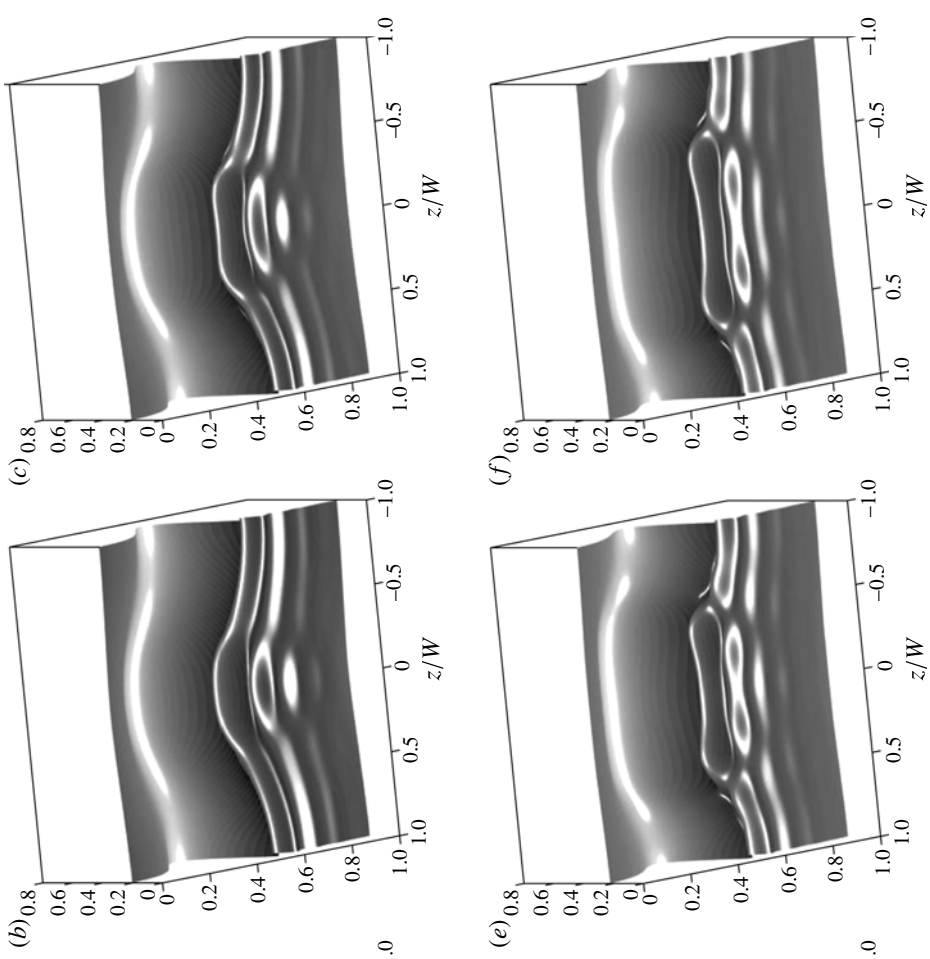


FIGURE 30. Case 3 (WRIBL): $Re^{lgt} = 15$, $f^{lgt} = 16$ Hz, $Ka = 509.5$, $L = 20.7$ mm, $W = 10.35$ mm. Time evolution of free surface (compare to figure 8): (*a*) $t = 0.095$ s; (*b*) $t = 0.16$ s; (*c*) $t = 0.19$ s; (*d*) $t = 0.23$ s; (*e*) $t = 0.28$ s; (*f*) $t = 0.30$ s.

https://doi.org/10.1017/jfm.2013.679 Published online by Cambridge University Press

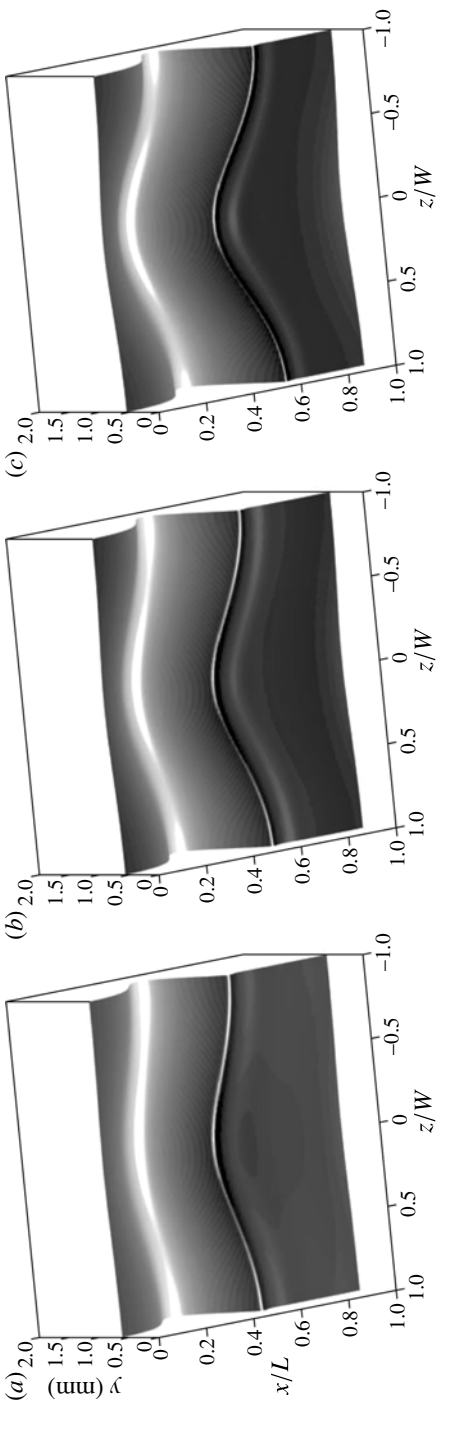


FIGURE 31. Case 4 (WRIBL): $Re^{fgt} = 6.2$, $f^{fgt} = 16.6$ Hz, $Ka = 17.8$, $L = 22$ mm, $W = 15$ mm. Time evolution of free surface (compare to figure 6): (*a*) $t = 0.09$ s; (*b*) $t = 0.12$ s; (*c*) $t = 0.16$ s; (*d*) $t = 0.19$ s; (*e*) $t = 0.23$ s; (*f*) $t = 0.28$ s.

https://doi.org/10.1017/jfm.2013.679 Published online by Cambridge University Press

topology are captured (qualitatively if not quantitatively) by the model for all cases, these long-time simulations can be regarded as physically sound.

REFERENCES

ADOMEIT, P. & RENZ, U. 2000 Hydrodynamics of three-dimensional waves in laminar falling films. *Intl J. Multiphase Flow* **26**, 1183–1208.

ALEKSEENKO, S. V., ANTIPIN, V. A., GUZANOV, V. V., KHARLAMOV, S. M. & MARKOVICH, D. M. 2005 Three-dimensional solitary waves on falling liquid film at low Reynolds numbers. *Phys. Fluids* **17**, 121704.

ALEKSEENKO, S. V., GUZANOV, V. V., MARKOVICH, D. M. & KHARLAMOV, S. M. 2012 Specific features of a transition from the regular two-dimensional to three-dimensional waves on falling liquid films. *Tech. Phys. Lett.* **38** (8), 739–742.

ALEKSEENKO, S. V., NAKORYAKOV, V. E. & POKUSAEV, B. G. 1994 *Wave Flow of Liquid Films*. Begell House.

BOYD, J. P. 2001 *Chebyshev and Fourier Spectral Methods*. Courier Dover.

BRACKBILL, J. U., KOTHE, D. B. & ZEMACH, C. 1992 A continuum method for modelling surface tension. *J. Comput. Phys.* **100**, 335–354.

BRAUER, H. 1956 Strömung und Wärmebergang bei Rieselfilmen. *VDI-Forschungsheft* **457** (22), 1–40.

BROOKE BENJAMIN, T. 1957 Wave formation in laminar flow down an inclined plane. *J. Fluid Mech.* **2**, 554–574.

BROOKE BENJAMIN, T. 1961 The development of three-dimensional disturbances in an unstable film of liquid flowing down an inclined plane. *J. Fluid Mech.* **10**, 401–419.

CHANG, H. C., CHENG, M., DEMEKHIN, E. A. & KOPELEVICH, D. I. 1994 Secondary and tertiary excitation of three-dimensional patterns on a falling film. *J. Fluid Mech.* **270**, 251–275.

CHANG, H. C., DEMEKHIN, E. A. & KALAIDIN, E. 1996*a* Simulation of noise-driven wave dynamics on a falling film. *AIChE J.* **42** (6), 1553–1568.

CHANG, H. C., DEMEKHIN, E. A., KALAIDIN, E. & YE, Y. 1996*b* Coarsening dynamics of falling-film solitary waves. *Phys. Rev.* E **54** (2), 1467–1477.

CHANG, H. C., DEMEKHIN, E. A. & KOPELEVICH, D. I. 1993 Nonlinear evolution of waves on a vertically falling film. *J. Fluid Mech.* **250**, 433–480.

CHENG, M. & CHANG, H. C. 1995 Competition between subharmonic and sideband secondary instabilities on a falling film. *Phys. Fluids* **7** (1), 34–54.

COHEN-SABBAN, J., GAILLARD-GROLEAS, J. & CREPIN, P.-J. 2001 Quasi-confocal extended field surface sensing. In *Optical Metrology Roadmap for the Semiconductor, Optical, and Data Storage Industries II* (ed. A. Duparre & B. Singh), Proc. SPIE, vol. 4449, pp. 178–183. SPIE.

DEMEKHIN, E. A., KALAIDIN, E. N., KALLIADASIS, S. & VLASKIN, S. YU. 2007*a* Three-dimensional localized coherent structures of surface turbulence. I. Scenarios of two-dimensional–three-dimensional transition. *Phys. Fluids* **19**, 114103.

DEMEKHIN, E. A., KALAIDIN, E. N., KALLIADASIS, S. & VLASKIN, S. YU. 2007*b* Three-dimensional localized coherent structures of surface turbulence. II. Solitons. *Phys. Fluids* **19**, 114104.

DEMEKHIN, E. A., KALAIDIN, E. N., KALLIADASIS, S. & VLASKIN, S. YU. 2010 Three-dimensional localized coherent structures of surface turbulence: model validation with experiments and further computations. *Phys. Rev.* E **82**, 036322.

DIETZE, G. F., AL-SIBAI, F. & KNEER, R. 2009 Experimental study of flow separation in laminar falling liquid films. *J. Fluid Mech.* **637**, 73–104.

DIETZE, G. F., LEEFKEN, A. & KNEER, R. 2008 Investigation of the back flow phenomenon in falling liquid films. *J. Fluid Mech.* **595**, 435–459.

DIETZE, G. F. & RUYER-QUIL, C. 2013 Wavy liquid films in interaction with a confined laminar gas flow. *J. Fluid Mech.* **722**, 348–393.

GEORGANTAKI, A., VATTEVILLE, J., VLACHOGIANNIS, M. & BONTOZOGLOU, V. 2011 Measurements of liquid film flow as a function of fluid properties and channel width: evidence for surface-tension-induced long-range transverse coherence. *Phys. Rev.* E **84**, 026325.

https://doi.org/10.1017/jfm.2013.679 Published online by Cambridge University Press

GJEVIK, B. 1970 Occurence of finite-amplitude surface waves on falling liquid films. *Phys. Fluids* **13** (8), 1918–1925.

HIRT, C. W. & NICHOLS, B. D. 1981 Volume of fluid (VOF) method for the dynamics of free boundaries. *J. Comput. Phys.* **39**, 201–225.

ISHIGAI, S., NAKANISI, S., KOIZUMI, T. & OYABU, Z. 1972 Hydrodynamics and heat transfer of vertically falling liquid films. *Bull. JSME* **15** (83), 594–601.

JOO, S. W. & DAVIS, S. H. 1992 Instabilities of three-dimensional viscous falling films. *J. Fluid Mech.* **242**, 529–547.

KALLIADASIS, S., RUYER-QUIL, C., SCHEID, B. & VELARDE, M. G. 2012 *Falling Liquid Films. (Applied Mathematical Sciences)*, vol. 176. Springer.

KAPITZA, P. L. 1948 Wave flow of thin layers of a viscous fluid. *Zh. Eksp. Teor. Fiz.* **3** (1), 3–28 (in Russian).

KUNUGI, T. & KINO, C. 2005 DNS of falling film structure and heat transfer via MARS method. *Comput. Struct.* **83** (6–7), 455–462.

LIU, J., PAUL, J. D., BANILOWER, E. & GOLLUB, J. P. 1992 Film flow instabilities and spatiotemporal dynamics. In *Proceedings of the First Experimental Chaos Conference* (ed. S. Vohra, M. Spano, M. Schlesinger, L. M. Pecora & W. Ditto), pp. 225–239. World Scientific.

LIU, J., PAUL, J. D. & GOLLUB, J. P. 1993 Measurements of the primary instabilities of film flows. *J. Fluid Mech.* **250**, 69–101.

LIU, J., SCHNEIDER, J. B. & GOLLUB, J. P. 1995 Three-dimensional instabilities of film flows. *Phys. Fluids* **7** (1), 55–67.

MALAMATARIS, N. A. & BALAKOTAIAH, V. 2008 Flow structure underneath the large amplitude waves of a vertically falling film. *AIChE J.* **54** (7), 1725–1740.

MALAMATARIS, N. A., VLACHOGIANNIS, M. & BONTOZOGLOU, V. 2002 Solitary waves on inclined films: flow structure and binary interactions. *Phys. Fluids* **14** (3), 1082–1094.

MANNEVILLE, P. 2004 *Instabilities, Chaos and Turbulence*. Imperial College Press.

MIYA, M., WOODMANEE, D. E. & HANRATTY, T. J. 1971 A model for roll waves in gas–liquid flow. *Chem. Eng. Sci.* **26**, 1915–1931.

MIYARA, A. 1999 Numerical analysis on flow dynamics and heat transfer of falling liquid films with interfacial waves. *Heat Mass Transfer* **35**, 298–306.

NAVE, J.-C. 2004 Direct numerical simulation of liquid films. PhD thesis, University of California.

NOSOKO, P., YOSHIMURA, P. N., NAGATA, T. & OYAKAWA, K. 1996 Characteristics of two-dimensional waves on a falling liquid film. *Chem. Eng. Sci.* **51** (5), 725–732.

NUSSELT, W. 1923 Der Wärmeaustausch am Berieselungskühler. *Zeitschrift des VDI* **67**, 206–210.

PARK, C. D. & NOSOKO, T. 2003 Three-dimensional wave dynamics on a falling film and associated mass transfer. *AIChE J.* **49** (11), 2715–2727.

PETVIASHVILI, V. I. & TSVELODUB, D. Y. 1978 Horseshoe-shaped solitons on a flowing viscous film of fluid. *Sov. Phys. Dokl.* **23**, 117–118.

POLLAK, T., HAAS, A. & AKSEL, N. 2011 Side wall effects on the instability of thin gravity-driven films – from long-wave to short-wave instability. *Phys. Fluids* **23**, 094110.

POPINET, S. 2009 An accurate adaptive solver for surface-tension-driven interfacial flows. *J. Comput. Phys.* **228**, 5838–5866.

PRADAS, M., KALLIADASIS, S., NGUYEN, P.-K. & BONTOZOGLOU, V. 2013 Bound-state formation in interfacial turbulence: direct numerical simulations and theory. *J. Fluid Mech.* **716**, R2.

PRADAS, M., KALLIADASIS, S. & TSELUIKO, D. 2012 Binary interactions of solitary pulses in falling liquid films. *IMA J. Appl. Maths* **77** (3), 408–419.

PRADAS, M., TSELUIKO, D. & KALLIADASIS, S. 2011 Rigorous coherent-structure theory for falling liquid films: viscous dispersion effects on bound-state formation and self-organization. *Phys. Fluids* **23**, 044104.

PRESS, W., TEUKOLSKY, S., VETTERLING, W. & FLANNERY, B. 1992 *Numerical Recipes in C – The Art of Scientific Computing*. Cambridge University Press.

PROSPERETTI, A. & TRYGGVASON, G. (Eds.) 2007 *Computational Methods for Multiphase Flow*. Cambridge University Press.

ROHLFS, W., DIETZE, G. F., HAUSTEIN, H., TSVELODUB, O. & KNEER, R. 2012 Experimental investigation into three-dimensional wavy liquid films under the influence of electrostatic forces. *Exp. Fluids* **53** (4), 1045–1056.

https://doi.org/10.1017/jfm.2013.679 Published online by Cambridge University Press

RUSCHE, H. 2002 Computational fluid dynamics of dispersed two-phase flows at high phase fractions. PhD thesis, Imperial College, University of London.

RUYER-QUIL, C. & MANNEVILLE, P. 2000 Improved modeling of flows down inclined planes. *Eur. Phys. J.* B **15** (2), 357–369.

RUYER-QUIL, C. & MANNEVILLE, P. 2002 Further accuracy and convergence results on the modeling of flows down inclined planes by weighted-residual approximations. *Phys. Fluids* **14** (1), 170–183.

SCHEID, B., KALLIADASIS, S., RUYER-QUIL, C. & COLINET, P. 2008*a* Interaction of three-dimensional hydrodynamic and thermocapillary instabilities in film flows. *Phys. Rev.* E **78**, 066311.

SCHEID, B., KALLIADASIS, S., RUYER-QUIL, C. & COLINET, P. 2008*b* Spontaneous channeling of solitary pulses in heated film flows. *Europhys. Lett.* **84** (6), 64002.

SCHEID, B., RUYER-QUIL, C. & MANNEVILLE, P. 2006 Wave patterns in film flows: modelling and three-dimensional waves. *J. Fluid Mech.* **562**, 183–222.

SHKADOV, V. YA. 1967 Wave flow regimes of a thin layer of viscous fluid subject to gravity. *Fluid Dyn.* **2** (1), 29–34.

SQUIRE, H. B. 1933 On the stability for three-dimensional disturbances of viscous fluid flow between parallel walls. *Proc. R. Soc. Lond.* A **142**, 621–628.

TAILBY, S. R. & PORTALSKI, S. 1962 The determination of the wavelength on a vertical film of liquid flowing down a hydrodynamically smooth plate. *Chem. Engng Res. Des.* **40**, 114–122.

TRIFONOV, Y. Y. 1990 Bifurcations of two-dimensional into three-dimensional wave regimes for a vertically flowing liquid film. *Fluid Dyn.* **25** (5), 741–745.

TRIFONOV, Y. Y. 2012 Stability and bifurcations of the wavy film flow down a vertical plate: the results of integral approaches and full-scale computations. *Fluid Dyn. Res.* **44** (5), 031418.

VLACHOGIANNIS, M., SAMANDAS, A., LEONTIDIS, V. & BONTOZOGLOU, V. 2010 Effect of channel width on the primary instability of inclined film flow. *J. Fluid Mech.* **22**, 012106.

YOUNGS, D. L. 1982 Time-dependent multi-material flow with large fluid distortion. In *Numerical Methods for Fluid Dynamics* (ed. K. W. Morton & M. J. Baines), pp. 273–285. Academic Press.

https://doi.org/10.1017/jfm.2013.679 Published online by Cambridge University Press